PREPRINT: Not peer reviewed. Submitted for publication in IEEE JSTARS.

Feature-Relative Deployment Optimisation of Ice-Tethered Buoy Arrays in the Southern Ocean

James H. Hepworth[1*] · **Edward Boje**[2] · **Amit Kumar Mishra**[3,4]

[1]Department of Mechanical Engineering, University of Cape Town, Cape Town, South Africa

[2]Department of Electrical Engineering, University of Cape Town, Cape Town, South Africa

[3]Faculty of Space Technology, AGH University of Krakow, Krakow, Poland

[4]University West, Trollhättan, Sweden

[*]Corresponding author: james.hepworth@uct.ac.za

Abstract The marginal ice zone of the Southern Ocean is critical for climate dynamics and sea-ice model validation, yet remains severely undersampled by in-situ platforms due to high operational costs and harsh conditions that make deployment challenging and limit ice-tethered buoy lifetime. Previous platform deployments have relied on heuristic deployment planning, leaving substantial room for systematic optimisation of observing array geometry. The core planning challenge is that the sea-ice edge can shift by hundreds of kilometres between years, rendering traditional fixed-coordinate optimisation strategies ineffective when future ice conditions are unknown. Further, data-driven optimisations risk overfitting to the specific drift product used for training, raising doubts about whether an optimised strategy encodes a genuinely transferable deployment rule. This paper presents a robust multi-objective optimisation framework that encodes buoy deployment locations relative to the dynamic ice-edge feature rather than fixed geographic coordinates, enabling the same genotype to adapt automatically to inter-annual ice variability. The framework uses NSGA-II to optimise spatial coverage and ship-operating costs. Training is performed using 39 years of Polar Pathfinder climatology (1979–2017), with blind validation on seven held-out test years (2018–2024) and cross-product transfer validation against two alternative observational drift products (DPGSIV AMSR2 and OSI-405-c). The proposed feature-relative strategy achieves 99.4% coverage retention on unseen test years, and outperforms fixed-coordinate, grid, random and historical fan baselines on coverage at lower cost than every reference. The strategy also transfers to alternative drift products with comparable performance, providing a quantified decision-support tool for pre-cruise buoy-array deployment planning under uncertain ice conditions.

Keywords: Buoy deployment · feature-relative encoding · NSGA-II · robust optimisation · sea ice observation

---

1 Introduction

1.1 Sea Ice Observation and the Deployment Challenge

Sea ice drift and deformation in the polar oceans play a critical role in the global climate system through heat and moisture exchange between the ocean and atmosphere [1], [2], [3]. Sea ice also supports unique ecosystems and represents an increasingly important region for shipping as ice cover changes. Accurate monitoring of sea ice motion and deformation in this region is essential for validating satellite products and improving climate models. Deformation of the ice, in turn, affects new ice growth, and so

an understanding of the location and timing of ice fracture is necessary to resolve the mechanical and energy balance of the ocean-ice-atmospheric system.

Deformation of the ice is inherently non-linear and observations from remote and in situ sensors have shown sea ice motion to be multifractal [4] and to be variable over multiple spatial scales [5], [6], where larger deformation rates are associated with smaller spatial scales [7], [8], [9]. Ice-tethered drifting buoys acting as Lagrangian trackers are the natural platform for measuring ice-field trajectories and for providing the data from which differential kinematic analysis (DKA) can be performed using triplets of buoys [3], [8], [10], [11]. DKA allows calculation of spatial and temporal variability parameters that describe ice rheology and deformation. The choice of analysis scale is important in DKA, as the scale of the triangle formed by the three buoys must be appropriate to resolve the deformation features of interest. Several studies have performed analyses in the range of 10–100 km [7], [9], [12], while more recent work has evaluated these at sub-10 km scales [5], [13]. Thus, ice-tethered buoys provide in-situ validation data for a variety of models and data products including sea-ice velocity products such as the Polar Pathfinder (PP) product from the NSIDC [14].

In the Southern Ocean (SO), these data remain sparse and the region remains severely undersampled due to the logistical challenges and high costs associated with deploying in-situ observing systems [15], [16]. Programmes such as the SO Seasonal Experiment (SCALE) deployed ice-tethered buoys in spring 2019 [17] and winter 2022 in the Atlantic sector of the SO, north of Queen Maud Land, with the aim of evaluating sea-ice drift and waves-in-ice behaviour in the region. Other notable expeditions include the Polynyas, Ice Production, and seasonal Evolution in the Ross Sea (PIPERS) in 2017 [18], [19], deployments on the *SA Agulhas II* Winter 2017 Cruise [20], [21], the Sea Ice Physics and Ecosystem EXperiment (SIPEX) in 2012 [22], and the Short Timescale Motion of Pancake Ice (STiMPI) deployment in 2000 [23]. Despite these efforts, the numbers of instruments deployed, and their lifespans achieved, pale in comparison to those in the Arctic where thousands of buoys have been deployed over the last 30 years, many of which survive across multiple seasons.

In the SO, these deployment operations incur substantial costs: for example, the SCALE expeditions cost approximately $48,500 per day in operational fees, with total cruise costs exceeding $679,000 for two-week missions from Cape Town, South Africa. There is consequently an inherent tension between maximising the spatial coverage of the MIZ region of interest (ROI) over the life of the buoys while minimising the operating costs required to deploy the array. Buoys deployed in the MIZ of the SO tend to have very short lifetimes due to the harsh environment, and extracting maximal value from them is of high importance. Further, the position of the ice edge can vary by hundreds of kilometres between years at the same latitudes. This makes it difficult to plan deployments that are robust to inter-annual variability in ice conditions. In the past, for SCALE missions, planning the deployment geometries of the ice-tethered buoys has relied on heuristic positioning methods, based on operator experience rather than systematic optimisation.

1.2 Deployment Planning Approaches in the Literature

Typically, the deployment of buoy networks is planned in oceanographic applications using a variety of approaches under the umbrella of Observing System Simulation Experiments (OSSEs) [24], [25], [26]. These involve simulating the deployment and performance of hypothetical observing systems on a simulated reference modelling the physics of the environment, and then comparing the measurement abilities of various configurations of the sensor network. These experiments have been applied to a wide variety of applications including moored, drifting, floating and mixed platform observing systems [25], [27], [28], [29]. The sensitivity of OSSEs to varying data assimilation methods and model physics has been highlighted in the literature [25] and so robust design depends on multi-system evaluation to ensure that the optimised deployment strategy is not overfitted to a single model or data product [30]. These caveats are especially important in the SO MIZ, where sparse observations, uncertain reanalyses, and incomplete model physics make classical OSSE validation harder, prompting interest in complementary planning approaches that remain useful when transferable forecast-impact estimates are difficult to obtain [15], [16].

The core challenge in deployment planning for these ice-tethered instruments is that future ice conditions are unknown at the time of planning, and the position of the sea-ice edge varies considerably from year to year. Traditional approaches for fixed ocean buoys use fixed geographic coordinates as decision variables to be optimised; however, these are inappropriate for the scenario where ice-edge position varies from year to year in corresponding seasons. For example, a deployment optimised for 2021′s ice-edge position, a high-ice year, would place buoys in open water during a low-ice year like 2022. Further, predictive models show large uncertainties in projected positions, and so optimisations resulting from them are low-confidence solutions. Historical data on sea-ice extent and velocity is available from a small number of sources, with only three providing daily (or near-daily) data: the PP product is a climate data record (CDR) produced by assimilating various data sources including AVHRR, AMSRE, SMMR, SSMI, and SSMI/S satellite remote sensors, International Arctic Buoy Program (IABP) buoy drift tracks, and NCEP/NCAR Reanalysis wind forecasts [31]. It provides daily sea ice velocity vectors, with full coverage of the SO on a 25 km grid, and spans the years 1978–2024. This product is the only full-coverage dataset providing a historical record of sea-ice velocity from before 2009. OSI-405 is the Southern Hemisphere low-resolution sea-ice drift product from OSI SAF [32] making use of the DMSP/ SSMIS, Metop/ASCAT and GCOM-W/AMSR-2 satellite inputs. It is reported every 48 h on a 62.5 km polar stereographic grid and spans 2009 to the present. Lastly, the Daily Polar Gridded Sea Ice Velocity (DPGSIV) record contains daily 24-hour sea-ice displacement vectors derived from AMSR2 on a 60 km Southern Hemisphere grid and is derived from brightness temperature data from AMSR-E and AMSR2 radiometers [33]. It spans 2012 to the present. These three products provide a sparse record of sea-ice drift and velocity, with only the PP product providing a long-term historical record. Thus, the scenario faced by researchers is challenging: costs are high, the environment extremely variable, forecasts are uncertain, and the data record is sparse. Further, and more subtly, given the dependence on small data records, a risk that accompanies any data-driven optimisation is that a strategy developed within a single drift product could achieve high performance by exploiting properties specific to that product (e.g. its drift structure, spatial support, or preprocessing) rather than by encoding a genuinely transferable deployment rule to the physical world.

Acknowledging these limitations, and motivated by the gap between high operational costs and the lack of robust deployment planning tools, this study addresses the optimisation problem through a feature-relative parameterisation of the search space and a train–test paradigm adapted from machine learning. Accordingly, this work presents a systematic genetic algorithm (GA)-based optimisation framework for planning the deployment of ice-tethered buoys in the SO that is robust to inter-annual variability in ice conditions and provides quantified decision support for operators.

1.3 Paper Overview and Contributions

This paper presents the following contributions:

1. A feature-relative genotype encoding for the deployment locations that automatically adapts to inter-annual variability. The decision variables to be optimised are defined relative to dynamic oceanographic features (the ice edge) rather than fixed coordinates. A strategy such as “deploy at 15 km along the ice edge, 5 km into the pack” automatically adapts to wherever the ice edge is located in any given year whereas optimising for geographic coordinates may place buoys at appropriate locations in one year, miss the ice entirely in another, or propose locations on solid ice that are physically impossible to reach in a given year.
2. A robust optimisation framework that optimises for the expected performance across 39 years of climate data (1979–2017) rather than single-year optimisation, with blind validation on 7 unseen test years (2018–2024) and genotype transfer validation across two alternative observational drift products.
3. A deployment strategy for cluster-constrained deployments that maintains valid triangular clusters for DKA compatibility through sequential relative encoding and constraint handling.

The framework enables quantified decision support: given a budget constraint, operators can select deployment strategies valid for any ice conditions expected in the deployment window.

At the core of this framework is the Non-dominated Sorting Genetic Algorithm II (NSGA-II) [34], a multi-objective evolutionary algorithm that searches the encoded deployment space under Pareto-dominance ranking, maintaining a diverse front of coverage–cost trade-offs rather than a single solution.

The paper is organised as follows. Section 2 presents the methodology employed including the data preparation, a description of the feature-relative genotype encoding, objectives and constraints, trajectory simulation, ship routing, the NSGA-II configuration, the blind-validation protocol, baseline strategies, and the cross-product transfer protocol. Section 3 states the experimental protocol governing all stochastic results. Section 4 reports the results, grouped by question, and Section 5 discusses these results and implications, and presents the conclusions.

2 Problem Formulation and Methods

2.1 Data Preparation and Study Domain

2.1.1 Dataset Preparation

The optimisation framework ingests a two-week window from 1–14 August across 46 years of PP daily ice motion vectors (1979–2024) [31], corresponding to the regular deployment schedule of the SCALE experiments. The 25 km grid is then bilinearly interpolated to 6.25 km resolution ($\times 4$ upsampling) for trajectory integration using a fourth-order Runge-Kutta scheme (Section 2.3). To account for sub-grid scale processes not resolved by the product (e.g. turbulence, inertial oscillations, tidal effects), a stochastic diffusion term is added to trajectories. The diffusion coefficient $K = 50\,\mathrm{m}^2/\mathrm{s}$ was estimated from observed sea ice deformation statistics in the Weddell Sea [35].

Data quality control and preprocessing ensure continuous, physically consistent velocity fields for trajectory generation. Non-finite values and unphysical fill flags in the raw velocity components are identified and removed, and the fields are converted to standard SI units (m/s). An explicit boolean validity mask ($\mathrm{valid} = \neg(\mathrm{isnan}(u) \vee \mathrm{isnan}(v))$) is constructed to isolate cells with active ice-motion vectors, and structurally missing values in the velocity arrays are set to zero: the product masks land, where ice motion is impossible, and ice-free ocean, where there is no ice to drift, and a zero fill encodes that (no ice, no drift) at both boundaries. Zero-filling also keeps the coastline and ice edge sharp instead of interpolating across this genuine discontinuity, which would smear inland and off-ice structure into the pack and create spurious convergence and divergence in a field that is subsequently analysed kinematically. All geometry is defined in the PP product's own projected frame, EASE-Grid South (Lambert azimuthal equal-area; EPSG:3409), with coordinates (x, y) in kilometres; latitude and longitude are used only to label maps. Valid deployment locations are extracted on the initial deployment date (1 August) from the same 6.25 km validity mask from which the ice edge is traced (Section 2.1.2): a cell is considered valid if it carries ice motion, lies inside the deployment ROI, lies on the pack side of the ice edge, and lies at least 10 km from the local ice-edge contour, an operational safety buffer measured as a distance in the projected frame. Fig. 1 shows the deployment ROI for this study and its position relative to the Antarctic continent.

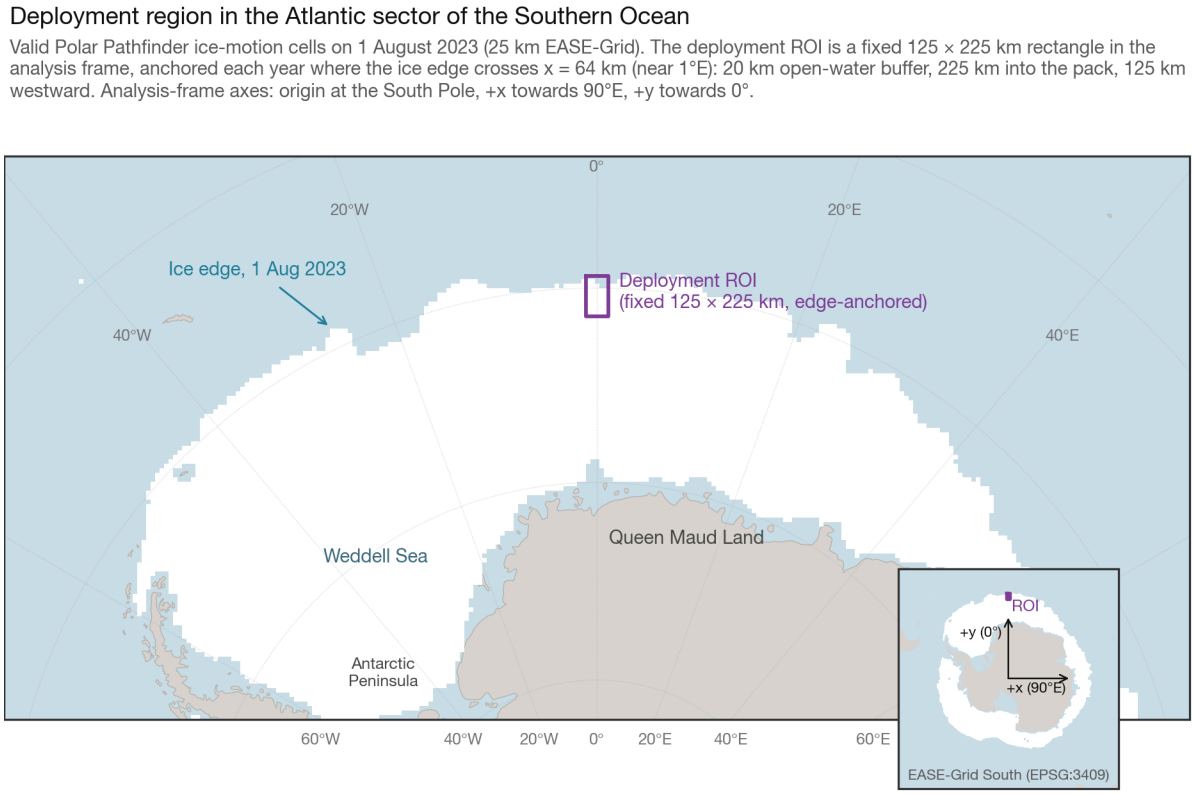


Fig. 1 Study region and valid Polar Pathfinder ice-motion support on 1 August 2023 (white, on a light-blue ocean), with the deployment ROI (purple): a fixed 125 × 225 km rectangle in the analysis frame, with its eastern side on the line $x = 64$ km (close to 1°E) and its top 20 km north of the year's most northerly ice-edge point within the rectangle's width. Arrows in the inset give the axes of the EASE-Grid South analysis frame from its origin at the South Pole: $+x$ points towards 90°E and $+y$ towards 0°, so on this map x increases eastward and y increases northward near the ROI. The inset locates the ROI relative to the Antarctic continent on the full Southern Hemisphere domain.

2.1.2 Ice Edge Definition and Processing

For each deployment date across all 46 years, the ice edge is extracted as the boundary of valid velocity vectors in the PP motion field on 1 August (where valid ice vectors transition to open-water NaN flags along the 15% sea-ice concentration contour). The validity mask is upsampled to the 6.25 km grid, and the pack outline is traced in the projected (x, y) frame as the longest 0.5 iso-contour of the mask, which discards short contours around detached ice. This outline encircles the continent, so the open-water edge is taken as the continuous stretch of the ring that lies inside the drift domain (Section 2.1.3.2) and contains its northernmost point. The stretch is smoothed with a moving-average filter (5–7 point window) to remove raster grid-staircase artefacts and uniformly resampled along its normalised arc length across $N = 500$ points, stored west to east. This smoothing removes small-scale noise while preserving the large-scale features of the ice edge, and the normalisation ensures comparable positions across years with different edge shapes and extents.

2.1.3 Regions of Interest and Spatial Discretisation

The optimisation framework defines two nested geographic regions of interest with distinct operational roles: an inner deployment ROI that serves both as the initial deployment zone and the target observational footprint, and an outer drift ROI that establishes the extended dynamic simulation domain within which Lagrangian trajectories are integrated.

2.1.3.1 Deployment ROI (Target Observation Footprint)

The candidate region for buoy deployment on 1 August is the region of the MIZ bounded approximately by 1°W to 1°E ($[-1°, 1°\text{E}]$). However, as the ice edge moves meridionally between years, bounding by longitude would result in ROIs that vary in area between years. To prevent this, a fixed-size rectangle in km (in the projected frame), anchored to the realised ice edge, is used so that it follows the feature between years while retaining a constant physical size. Its eastern side lies on the anchor line $x = 64$ km, and the northernmost crossing of that line by the ice edge is defined as the $w = 0$ contact point (64 km is the median 1°E crossing of the climatology). The rectangle extends 125 km west of the anchor line; its top lies 20 km north of the most northerly ice-edge point within that 125 km corridor (an operational open-water safety buffer), and it extends 225 km south from there into the ice pack, a depth encompassing the active breadth of the MIZ [36]. Where the edge runs east–west across the corridor the $w = 0$ point sits just below the top of the rectangle; where the edge climbs northward west of the anchor line, the $w = 0$ point sits correspondingly deeper inside it. This sector matches the primary cruise tracks of recent SCALE expeditions departing from Cape Town.

Importantly, the deployment ROI serves a dual function in the formulation: it defines the geographic envelope within which buoys must physically be placed on 1 August, and it defines the designated target observation footprint over which spatial coverage (f_1; Section 2.2.3) is evaluated throughout the deployment.

2.1.3.2 Drift ROI (Simulation Domain)

The drift domain is a fixed box in the projected frame, $-145 \leq x \leq 145$ km and $2970 \leq y \leq 4150$ km (approximately 2°W–2°E and 63°–52°S). This provides a generous spatial buffer around the 125 km wide deployment corridor, ensuring that buoys advected by the prevailing eastward and northward circumpolar drift remain within valid velocity fields throughout the 14-day evaluation window. Trajectories are integrated across the full 14-day horizon regardless of whether buoys drift outside the deployment corridor; no artificial clipping or trajectory termination occurs at the corridor boundaries.

2.1.3.3 Evaluation Grid Discretisation and Boundary Behaviour

To evaluate the proximity component of the coverage objective (J_{cov}, and hence f_1; Section 2.2.3), the deployment ROI is discretised into a regular 25 km grid in projected EASE-Grid South (x, y) space. The grid resolution is set to $\Delta x = \Delta y = 25$ km, matching the native nominal resolution of the PP motion product.[1] Because the deployment ROI is a fixed-size rectangle in the projected plane, the evaluation grid has a constant number of cells ($N_{\text{grid}} = 45$, a 5×9 lattice) and a constant bounding-box diagonal $D_{\max} = \sqrt{(x_{\max} - x_{\min})^2 + (y_{\max} - y_{\min})^2} \approx 257$ km in every year of the climatology. Therefore, the proximity score J_{cov} is directly comparable across years, since its normaliser is constant by construction. Additionally, an operational arrival waypoint $\boldsymbol{g}_{\text{entry}}$ is defined at the top of the anchor line $x = 64$ km, on the northern open-water boundary of the ROI, fixing the starting point from which the vessel transits south to contact the ice edge.

2.1.4 Train/Test Split

Following this, the August 1–14 annual windows from the PP product are split into a training and a testing set, which allows optimisation to be performed using part of the record and then the candidate solution to be evaluated on a separate part of the record which is unseen to the optimiser. Table 1 shows the detail of this division.

[1] While the velocity field is bilinearly upsampled to 6.25 km to ensure smooth numerical advection during RK4 trajectory integration, coverage is evaluated at the motion product's native 25 km physical resolution. Because the mean minimum distance metric is a Riemann approximation of the continuous spatial coverage integral, the 25 km grid provides rank-invariant fitness evaluations (Spearman rank correlation $\rho > 0.998$ against a 6.25 km evaluation grid) while avoiding a $16\times$ computational overhead in the multi-decadal evolutionary loop.

Table 1 Details of the Train/Test split of the PP product

Set	Years	Purpose
Training	1979–2017 (39 years)	Ensemble evaluation across historical climatological conditions
Testing	2018–2024 (7 years)	Blind out-of-sample validation under unseen ice regimes

The training set comprises all 39 years from 1979 to 2017, spanning diverse ice conditions and capturing multidecadal variability in ice-edge position, drift speeds, and deformation regimes; the 1 August ice edge crosses the anchor line in every year, so a deployment ROI exists for each (Section 2.1.3.1). Rather than optimising fixed buoy coordinates for a single specific year, the framework evaluates each candidate deployment rule across all 39 training years simultaneously. In this ensemble formulation, the training years serve as empirical realisations drawn from the underlying climatological distribution of Southern Ocean winter conditions. Simulating trajectories across all 39 years constructs an empirical probability density function (PDF) of coverage and cost outcomes for each candidate strategy. The optimiser then evaluates and ranks candidate solutions based on their expected performance across this distribution, identifying robust decision rules that perform reliably regardless of the specific ice configuration encountered in any deployment year. The remaining 7 years (2018–2024) are held out entirely as a blind test set, representing recent environmental conditions to assess whether the learned deployment rules successfully generalise to unseen years without performance degradation.

2.2 Problem Reformulation

2.2.1 Sequential Feature-Relative Genotype Encoding

To enable adaptation to ice variability while maintaining valid cluster geometries, a sequential relative encoding is employed for the genotype of the GA. A primary, anchor cluster is defined relative to the intersection of the ice edge and the eastern boundary of the ROI. From this anchor (i.e. Cluster 1), the remaining clusters are defined as a chain relative to the centroid of the first cluster. Therefore, the genotype for n_C clusters is defined as follows:

$$\boldsymbol{z} = \left[\underbrace{w d_1 \alpha_1 \theta_1 s_1}_{\text{Cluster 1}}, \underbrace{d_2 \varphi_2 \theta_2 s_2}_{\text{Cluster 2}}, ..., \underbrace{d_{n_C} \varphi_{n_C} \theta_{n_C} s_{n_C}}_{\text{Cluster } n_C} \right] \tag{1}$$

The variables of Cluster 1 are detailed in Table 2 below. The scale s_k is restricted to the range 10–30 km to isolate a mesoscale range that is appropriate for DKA. A lower limit of 10 km is consistent with the scale at which deformation has traditionally been resolved in previous studies, and it avoids the sub-10 km regime where recent work shows a change in deformation behaviour and weaker support for scale-invariant interpretations [5], [6], [13]. The upper limit of 30 km keeps the clusters within the mesoscale range while reducing the averaging effects that could mask local gradients over larger scales [8], [9], [35].

Table 2 Cluster 1 (ice-edge feature-relative) genotype parameters and bounds.

Variable	Description	Range
w	Normalised arc-length position along ice edge contour within ROI, measured westward from the eastern ROI boundary ($w = 0$)	$[0, 1]$
d_1	Distance of the Cluster 1 centroid from the anchor point on the ice edge	$[0, 50]$ km
α_1	Heading of the d_1 displacement, measured clockwise from the grid $+y$ axis	$[0, 2\pi]$
θ_1	Triangle orientation, measured clockwise from the grid $+y$ axis	$[0, 2\pi]$
s_1	Scale (vertex spacing / triangle side length)	$[10, 30]$ km

Similarly, Table 3 details the variables of each chain cluster. Inter-cluster distance is bounded by the breadth of the MIZ, which extends up to 200 km into the ice field from the edge [36]. The lower limit

of 50 km is set to prioritise the spread of clusters across the MIZ. s_k follows the same limits as s_1 for consistency. All angular genes (α_1, θ_k, φ_k) are measured clockwise from the grid $+y$ axis of the projected analysis frame (EASE-Grid South); they are grid angles rather than angles relative to geographic north, and the navigation-relevant compass directions and leg distances are derived separately from the decoded positions when the waypoint schedule is produced (Table 8) ahead of implementation.

Table 3 Subsequent cluster ($k > 1$) genotype parameters and bounds.

Variable	Description	Range
d_k	Distance from Cluster $k-1$ centroid	$[50, 200]$ km
φ_k	Heading from Cluster $k-1$ centroid, measured clockwise from the grid $+y$ axis	$[0, 2\pi]$
θ_k	Triangle orientation, measured clockwise from the grid $+y$ axis	$[0, 2\pi]$
s_k	Scale (vertex spacing / triangle side length)	$[10, 30]$ km

This genotype is expressed diagrammatically in Fig. 2 below.

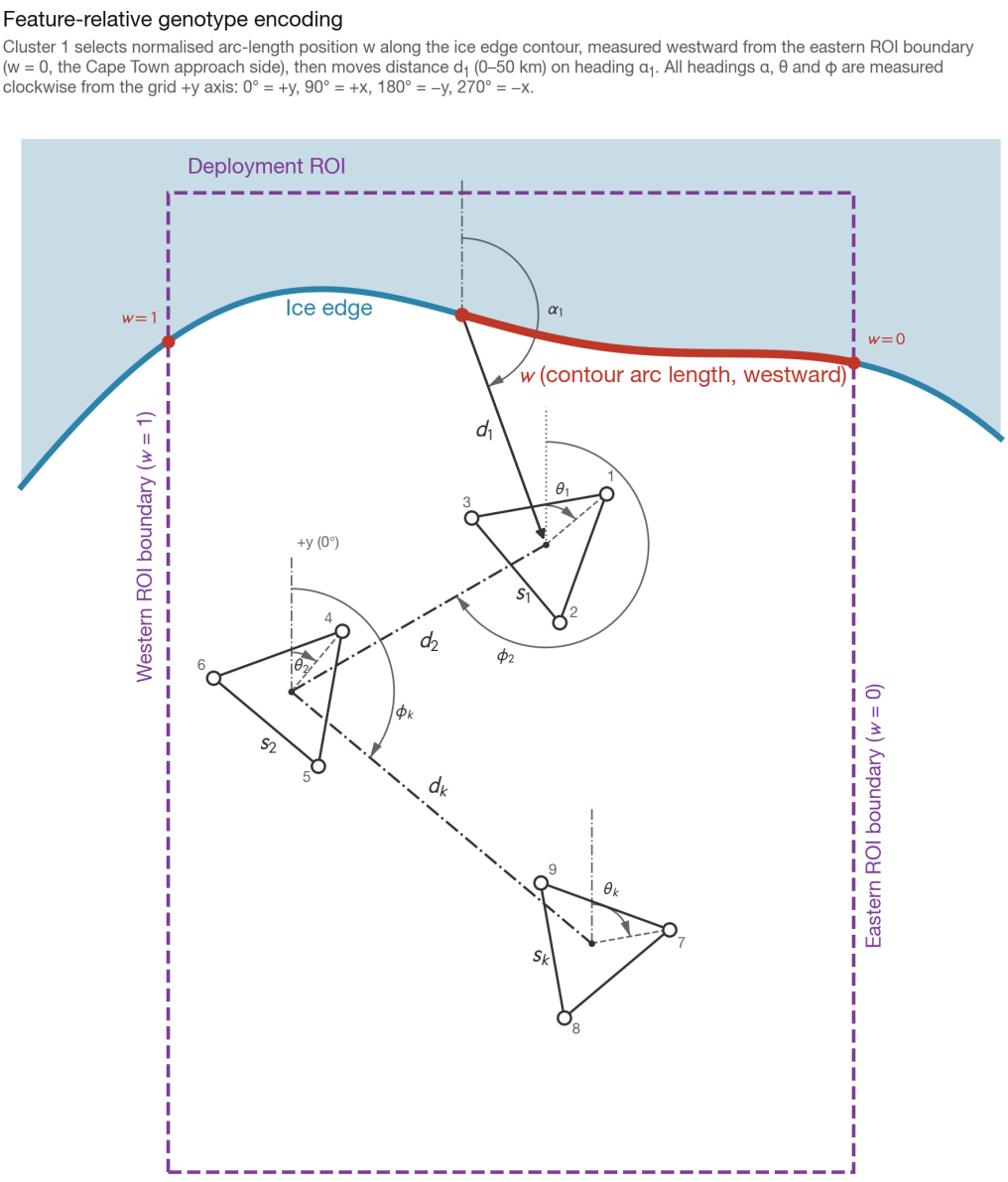


Fig. 2 Feature-relative genotype encoding. Cluster 1 selects a normalised east–west position w along the ice edge ($w = 0$ at the eastern ROI boundary, matching the approach from Cape Town), anchors to the corresponding ice-edge point, and moves distance d_1 on heading α_1 to the Cluster 1 centroid. Subsequent cluster centroids are chained by distance d_k on heading φ_k. All angular genes α_1, θ_k and φ_k are measured clockwise from the grid $+y$ axis of the analysis frame. Each cluster is an equilateral triangle with side length s_k; vertices 1–3 denote buoy order.

2.2.2 Genotype-to-Phenotype Mapping

The mapping from genotype to phenotype is applied independently for each year in the evaluation, using that year's realised 1 August ice edge. The mapping is stated as an operational placement procedure in order to keep the optimised strategies directly interpretable for cruise planning. It must be emphasised, however, that this procedure is a geometric construction, not the vessel's transit route: the phenotype it produces is solely the set of n_B buoy deployment positions, and the ship route used to cost a deployment is derived from those positions separately. The mapping is as follows.

1. First, the normalised arc-length gene w parameterises the ice edge contour, with $w = 0$ at the contour's intersection with the eastern ROI boundary and w increasing westward; the value w locates the anchor waypoint $\left(x_{\text{edge}(w)}, y_{\text{edge}(w)}\right)$. Operationally this corresponds to tracking the ice edge in open water westward for a known geographic distance (recoverable from w and the local contour length) from

the eastern ROI boundary. From the anchor waypoint, the centroid of the first cluster $\boldsymbol{c}_1$ is placed a distance $d_1 \in [0, 50]$ km away on heading α_1 (measured clockwise from the grid $+y$ axis):

$$\boldsymbol{c}_1 = \left(x_{\text{edge}(w)}, y_{\text{edge}(w)}\right) + d_1(\sin\alpha_1, \cos\alpha_1) \tag{2}$$

The heading is unrestricted, so the genotype can describe a placement in open water or too close to the edge. Such placements are not corrected by the decoder; instead, they make the genotype infeasible through the on-ice constraint of Section 2.2.3, and the search learns headings and distances that place Cluster 1 in the pack in every year.

2. Each subsequent centroid is placed relative to the preceding cluster, at distance d_k on heading φ_k (measured clockwise from the grid $+y$ axis):

$$\boldsymbol{c}_k = \boldsymbol{c}_{k-1} + d_k(\sin(\varphi_k), \cos(\varphi_k)) \tag{3}$$

3. Each centroid is clipped to the deployment ROI, with a margin of one triangle circumradius so that the whole triad lies inside the rectangle.

4. Vertices are then placed around each centroid using heading θ_k (measured clockwise from the grid $+y$ axis) and scale s_k. The first vertex is placed at heading θ_k, with subsequent vertices at $\theta_k + 120°$ and $\theta_k + 240°$ to form an equilateral triangle.

The decoded positions are used exactly as the genes place them, and whether each buoy can be deployed, on a valid ice cell, is tested by the on-ice constraint (Section 2.2.3). Because the placement rule is defined relative to the realised ice edge, the same genotype yields different geographic positions when the ice edge moves between years, while always remaining straightforward to execute in the field: navigate along the visible ice edge to the anchor waypoint, then turn onto a fixed heading for a fixed distance.

The phenotype, then, comprises the n_B buoy deployment positions $\{\boldsymbol{b}_i\}$ decoded for a given year, while the ship's transit route is not genetically encoded and carries no heritable information. Instead, the route is a derived quantity, computed a posteriori from the decoded positions. Costing for the transit route begins at the $w = 0$ contact point (i.e. the intersection of the ice edge with the eastern ROI boundary, the anchor line) so the costed route is: (i) an edge-tracking leg westward along the visible ice edge from $w = 0$ to the anchor waypoint, of length $w \times L_{\text{edge}}$ where L_{edge} is the arc length of the in-ROI contour segment; and (ii) a deployment tour from the anchor waypoint through all buoy positions, solved as a small Travelling Salesman Problem (TSP) with the first buoy fixed as the one nearest the anchor (nearest-neighbour initialisation followed by 2-opt improvement, with free ordering thereafter and no return leg; see Section 2.4). The open-water approach transit to the deployment region is excluded from the costing, so all strategies are compared from the moment the vessel arrives at the ice edge on the eastern ROI boundary. The resulting minimum route distance $D_{\text{route}(\boldsymbol{z})}$ determines the cost objective.

2.2.3 Objective Functions and Cluster Validity

The multi-objective genetic algorithm simultaneously optimises two competing criteria: maximising the effective spatial observation coverage of the marginal ice zone ($f_1 \in [0, 1]$) while minimising the operational ship deployment charter cost (f_2). Coverage is developed as a composite fitness function consisting of a base proximity score penalised by a set of constraints that promote triangular clusters with appropriate separation and shorter deployment times. In general, buoys are deployed as part of broader expedition goals, not all of which share the MIZ as the ROI. Deployment windows that take under 48 hours (the approximate duration usually allocated to MIZ operations on recent SCALE expeditions) are therefore considered operationally feasible, while longer deployments incur a penalty.

2.2.3.1 Coverage Objective (J_{cov})

Accordingly, base coverage is quantified by how closely the ensemble of buoy trajectories samples the discretised deployment ROI. The specific metric is the mean minimum distance from each grid cell within the ROI to the nearest trajectory point. This was selected after evaluating five candidate formulations: binary coverage fraction, ensemble spread, visit uniformity, minimax distance, and the mean minimum

distance adopted here (Appendix A). Mean minimum distance was preferred because it provides a smooth fitness landscape, directly targets proximity of observations to every part of the ice-edge zone, and averages robustly across the multi-year training climatology without year-specific threshold tuning. This objective function is defined as follows.

Let $\boldsymbol{g}_k \in \mathbb{R}^2$ $(k = 1, ..., N_{\text{grid}})$ denote the centroid coordinates of the N_{grid} regular 25 km evaluation grid cells discretising the target observation region (Section 2.1.3). For a deployment of n_B buoys whose trajectories are integrated over a time horizon $\mathcal{T} = \{t_1, ..., t_T\}$, the mean minimum distance from every grid cell to the nearest trajectory point is:

$$\bar{d}_{\min(\boldsymbol{z})} = \frac{1}{N_{\text{grid}}} \sum_{k=1}^{N_{\text{grid}}} \min_{i \in \{1,...,n_B\}} \min_{t \in \mathcal{T}} \left\| \boldsymbol{g}_k - \boldsymbol{r}_i(t) \right\|_2, \tag{4}$$

where $\boldsymbol{r}_i(t)$ is the position of buoy i at time t, in kilometres. This physical distance is rescaled against the maximum bounding-box diagonal $D_{\max}$ of the evaluation domain to give a dimensionless base coverage score in $[0, 1]$:

$$J_{\text{cov}(\boldsymbol{z})} = \max\left(0, 1 - \frac{\bar{d}_{\min(\boldsymbol{z})}}{D_{\max}}\right), \tag{5}$$

where $J_{\text{cov}} = 1$ corresponds to complete, zero-distance spatial coverage of the target footprint and higher values are better.

The relationship between the internal evaluation cells $\boldsymbol{g}_k$ and buoy trajectories advecting outside the deployment region governs how coverage is accumulated. The proximity metric calculates the minimum Euclidean distance from each target cell $\boldsymbol{g}_k$ to every trajectory point across all $n_B = 9$ buoys and all integration time steps: $\min_{i,t} \left\| \boldsymbol{g}_k - \boldsymbol{r}_i(t) \right\|_2$. Trajectory points generated after a buoy has exited the region are not discarded; they remain part of the search set. The effect of these post-exit points depends on the position of a cell in the grid. Cell centroids lie 12.5 km inside the ROI boundary, and each further row or column adds 25 km. A trajectory point outside the ROI is therefore at least 12.5, 37.5 and 62.5 km from the cells in the first, second and third row or column from the nearest boundary. If a buoy exits across any boundary and stays near it, its post-exit points can set the minimum distance for the adjacent boundary strip. This proximity is a real sample of the ice near the ROI, not an artefact of the metric. The benefit decreases by 25 km per row or column into the grid, and points that drift far downstream contribute nothing. A deployment whose buoys leave the ROI early can thus keep low distances along the boundary strips, but the deeper cells stay far from all trajectories. The mean minimum distance over all 45 cells stays large, and J_{cov}, and hence f_1, stays low. Conversely, genotypes whose deployed arrays linger within, or sweep comprehensively across, the target observation footprint are favoured by NSGA-II.

2.2.3.2 Cluster Geometric Validity (v_{cluster})

To ensure that buoy triads remain valid for mesoscale DKA of sea-ice strain rates, three geometric constraints are applied that aim (1) to initially place buoys in the range of 10–30 km apart, (2) to maintain cohesion throughout the drift period, and (3) to initially deploy buoys in roughly equilateral triangles. Accordingly, each triangular cluster $C_k = \{b_1, b_2, b_3\}$ $(k \in \{1, ..., n_C\})$ is evaluated against the following constraints:

1. Initial Deployment Separation (v_{init}): At deployment $(t = 0)$, pairwise distances $d_{ij}(0) = \left\| \boldsymbol{r}_i(0) - \boldsymbol{r}_j(0) \right\|_2$ between buoys in cluster C_k must satisfy $d_{\min} \leq d_{ij}(0) \leq d_{\max,\text{init}}$ $(10 \leq d_{ij} \leq 30$ km) in the simulation environment:

$$p_{ij}^{\text{init}} = \begin{cases} 1 & \text{if } d_{\min} \leq d_{ij}(0) \leq d_{\max,\text{init}} \\ \left(\frac{d_{ij}(0)}{d_{\min}}\right)^2 & \text{if } d_{ij}(0) < d_{\min} \\ \frac{d_{\max,\text{init}}}{d_{ij}(0)} & \text{if } d_{ij}(0) > d_{\max,\text{init}} \end{cases}. \tag{6}$$

Here a quadratic penalty is applied below the minimum distance to harshly penalise configurations where buoys are too close for DKA to be feasible at the mesoscale. Above the maximum initial separation, a linear penalty is applied to more softly penalise configurations where buoys are further apart than the perceived ideal – this is done to acknowledge the fact that initial separation marginally above the $d_{\text{max,init}}$ is still DKA valid at the mesoscale and the softer linear penalty helps preserve genetic diversity in the early phases of the optimisation. The cluster's initial-separation score is the mean over its three buoy pairs,

$$v_{\text{init}} = \frac{1}{3} \sum_{i<j} p_{ij}^{\text{init}}. \tag{7}$$

The mean form matches the drift term below so that both aggregate the per-pair penalties identically.

2. Drift Cohesion (v_{drift}): Throughout the 14-day drift period, buoys must maintain cohesion without excessive divergence ($d_{\text{max,drift}} = 50$ km):

$$p_{ij}(t) = \begin{cases} 1 & \text{if } d_{\text{min}} \le d_{ij}(t) \le d_{\text{max,drift}} \\ \left(\frac{d_{ij}(t)}{d_{\text{min}}}\right)^2 & \text{if } d_{ij}(t) < d_{\text{min}} \\ \frac{2d_{\text{max,drift}}}{d_{ij}(t)+d_{\text{max,drift}}} & \text{if } d_{ij}(t) > d_{\text{max,drift}} \end{cases} \tag{8}$$

and the cohesion score is the mean of these per-pair penalties over the three pairs and the T integration steps:

$$v_{\text{drift}} = \frac{1}{T} \sum_{t=1}^{T} \left(\frac{1}{3} \sum_{i<j} p_{ij}(t) \right). \tag{9}$$

The excess-separation decay above $d_{\text{max,drift}}$ is weighted by one half relative to the initial-separation term, so the drift penalty penalises divergence more gently than a poor initial geometry. The same quadratic-linear penalty form is applied to $p_{ij}(t)$ to maintain consistency with the initial-separation term. This asymmetry reflects the fact that a poor initial geometry is a direct genotype-attributable placement error, whereas divergence during drift is partly imposed by the ice motion field rather than by the encoded positions, so the penalty should not be so harsh as to eliminate otherwise promising deployments with divergence greater than intended.

3. Non-Collinearity Triangle Shape (v_{shape}): To prevent clusters of buoys from forming collinear strings on deployment (which prevents calculating 2D strain rate tensors), the linearity ratio R is defined from sorted edge lengths $l_1 \le l_2 \le l_3$:

$$R = \frac{l_3}{l_1 + l_2} \tag{10}$$

For an equilateral triangle, $R = 0.5$; for a degenerate line, $R = 1.0$. A threshold $\tau = 0.6$ penalises near-collinear geometries:

$$v_{\text{shape}} = \begin{cases} 1 & \text{if } R \le \tau \\ 1 - (R - \tau) & \text{if } R > \tau \end{cases} \tag{11}$$

A mild continuous decay above $R > \tau$ is used: while equilateral triangles are the preferred geometry for DKA, the requirement is simply that $R \le 1$. Steeper alternatives are possible, but the mild decay is sufficient to guide the search away from collinear configurations while preserving genetic diversity.

The feature-relative encoding satisfies the equilateral preference by construction and the decay is not realised here. The decoder deploys every triad as an equilateral triangle of side s_k and never moves individual buoys, so $R = 0.5$ and $v_{\text{shape}} = 1$ for every genotype. However, the decay case is retained for the purpose of evaluating the baselines of Section 2.7, which snap individual buoys to valid cells and hence produce non-equilateral triads. Shape conditioning is required only at deployment: drift may

stretch an initial equilateral triad, which the cohesion term regulates through the separation bounds $\left[d_{\min}, d_{\max,\text{drift}}\right]$ alone.

The combined cluster validity score is the arithmetic mean across the three components for each cluster C_k: $v_k = \frac{1}{3}\left(v_{\text{init}} + v_{\text{drift}} + v_{\text{shape}}\right)$, and the ensemble cluster validity is therefore given by:

$$v_{\text{cluster}} = \frac{1}{n_C} \sum_{k=1}^{n_C} v_k \tag{12}$$

Table 4 summarises the geometric validity constraints and their mathematical formulations.

Table 4 Summary of geometric validity and operational cluster constraints.

Constraint	Mathematical Formulation	Threshold
Minimum separation	$\left\|\boldsymbol{r}_i - \boldsymbol{r}_j\right\|_2 \geq d_{\min}$	10 km
Maximum initial separation	$\left\|\boldsymbol{r}_i - \boldsymbol{r}_j\right\|_2 \leq d_{\text{max, init}}$	30 km
Maximum drift separation	$\left\|\boldsymbol{r}_i(t) - \boldsymbol{r}_j(t)\right\|_2 \leq d_{\text{max, drift}}$	50 km
Non-collinearity shape	$\frac{l_3}{l_1+l_2} \leq \tau$	$\tau = 0.6$
Inter-cluster spacing	$\left\|\boldsymbol{c}_k - \boldsymbol{c}_{k'}\right\|_2 \geq d_{\text{inter}}$	50 km

2.2.3.3 Inter-Cluster Spacing and Deployment Duration Penalties

Two operational penalties further refine the coverage objective: the inter-cluster separation penalty and the deployment time window penalty. The inter-cluster separation factor (v_{inter}) ensures that cluster centroids $\boldsymbol{c}_k$ maintain a minimum separation of $d_{\text{inter}} = 50$ km to avoid spatial redundancy between different clusters:

$$v_{\text{inter}} = \begin{cases} 1 & \text{if } d \geq d_{\text{inter}} \\ \left(\frac{d}{d_{\text{inter}}}\right)^2 & \text{if } d < d_{\text{inter}} \end{cases} \tag{13}$$

where $d = \min_{k \neq k'} \left\|\boldsymbol{c}_k - \boldsymbol{c}_{k'}\right\|_2$ is the smallest pairwise centroid distance across the three triads. The rationale is to push the optimiser to spread the clusters across the breadth of the marginal ice zone: two triads placed within roughly 50 km of one another sample essentially the same patch of ice, and their trajectories would add little to the coverage objective (f_1) that a single triad would not already provide. The threshold d_{inter} is an operational spacing chosen to be commensurate with the drift-cohesion limit ($d_{\max,\text{drift}} = 50$ km). It is not derived from, and does not claim to match, the spatial decorrelation scale of the drift field. The quadratic penalty form $\left(\frac{d}{d_{\text{inter}}}\right)^2$ grows smoothly but steeply as the closest pair draws together. This allows mild proximity to be lightly penalised while near-coincident clusters are strongly driven apart. This gives the constraint a well-behaved gradient rather than a hard cutoff, consistent with the smooth-landscape design of the coverage objective. When $d \geq d_{\text{inter}}$ the term is exactly unity and exerts no effect on the fitness.

Secondly, the deployment time window factor (v_{deploy}) ensures that the costed route (edge-tracking leg plus buoy tour) does not exceed the 48-hour operational deployment window. This is given by:

$$v_{\text{deploy}} = \exp\left(-\frac{\max(0, T_{\text{total}} - 48)}{6}\right), \tag{14}$$

where $T_{\text{total}} = \frac{D_{\text{route}(\boldsymbol{z})}}{v_{\text{ship}}}$ is the total sailing time required to execute the deployment, derived from the same route distance D_{route} that drives the cost objective f_2. A deployment that fits within the 48-hour window is considered operationally feasible and earns the full term ($v_{\text{deploy}} = 1$). Deployments that overrun are penalised by an exponential decay with a 6-hour characteristic time: each additional hour of overrun shrinks the term smoothly, reaching $e^{-1} \approx 0.37$ at 54 h and $e^{-2} \approx 0.14$ at 60 h. Because v_{deploy} multiplies the coverage fitness f_1, an over-window deployment forfeits coverage credit; the linear per-hour cost of

the overrun is already priced by f_2, but f_2 alone would admit over-window solutions whose coverage gain justifies the additional expense. The 48 h window is an operational feasibility limit rather than a monetary one, so v_{deploy} removes that trade-off by decaying steeply in the overrun. The soft exponential form, rather than a hard step at 48 h, preserves a smooth gradient so the search can still discriminate between, and trade off, marginally over-window solutions.

2.2.3.4 Composite Coverage Fitness

The final penalised coverage fitness is the base proximity score reduced by the constraint terms, and is maximised:

$$f_1(\boldsymbol{z}) = J_{\text{cov}(\boldsymbol{z})} \times v_{\text{cluster}(\boldsymbol{z})} \times v_{\text{inter}(\boldsymbol{z})} \times v_{\text{deploy}(\boldsymbol{z})} \times v_{\text{ice}(\boldsymbol{z})}, \quad f_1 \to \max \tag{15}$$

where $v_{\text{ice}} = 1 - \frac{n_{\text{off}}}{n_B}$ is the fraction of the n_B buoys that decode inside a valid deployment cell (Section 2.1.1). Since every term $v \in [0, 1]$, a fully valid deployment retains $f_1 = J_{\text{cov}}$, while a half-valid geometry halves it. The product shapes the objective continuously; it does not by itself decide which genotypes may occupy the Pareto front, and that distinction is made explicit next.

2.2.3.5 Feasibility and Constrained Domination

A genotype whose triads violate the DKA geometric requirements can still be deployed if every buoy is on ice, but its triads cannot support DKA, so it does not meet the observing goal. A penalty alone cannot remove such a genotype from the Pareto front: the penalty only lowers f_1, and an infeasible array that is cheaper than every feasible array stays non-dominated on f_2, whatever its coverage.

Feasibility is therefore a constraint, but only for the conditions that the encoded positions control: initial separation, triangle shape, inter-cluster spacing, the deployment window, and deployment on valid ice. Drift cohesion stays a penalty inside f_1 only, because the ice motion field, not the deployment geometry, mostly decides whether a triad stays within $\left[d_{\min}, d_{\max,\text{drift}}\right]$ over fourteen days (Section 2.2.3.2). The decoder applies no repair, so the genotype itself must put every buoy on a valid ice cell (Section 2.1.1). Let $\bar{v}_{\text{init}}$ and $\bar{v}_{\text{shape}}$ be the cluster means of the related validity factors, and $n_{\text{off}(\boldsymbol{z},\omega)}$ the number of buoys that decode off valid ice in year ω. The constraint violation in year ω is

$$v(\boldsymbol{z}, \omega) = (1 - \bar{v}_{\text{init}}) + \left(1 - \bar{v}_{\text{shape}}\right) + (1 - v_{\text{inter}}) + \left(1 - v_{\text{deploy}}\right) + \lambda_{\text{ice}} n_{\text{off}(\boldsymbol{z},\omega)} \geq 0, \tag{16}$$

which is zero when all five conditions hold. The fraction of buoys on valid ice also multiplies f_1, with v_{cluster}, v_{inter} and v_{deploy}, so an undeployable buoy loses its share of coverage. Over the training ensemble, $v^{\text{rob}(\boldsymbol{z})} = \frac{1}{N_{\text{train}}} \sum_{\omega \in \text{ Train}} v(\boldsymbol{z}, \omega)$. Each term is non-negative, so a zero mean requires every training year to be feasible. A tolerance $v^{\text{rob}} \leq 0.02$ therefore lets a well-formed array pass if, for example, one year's ice-edge position pushes the route past 48 h. Deployability gets no such tolerance. With $\lambda_{\text{ice}} = 100$, one off-ice buoy in one training year raises v^{rob} to about 2.6, far above the tolerance. Every member of the reported front thus puts all nine buoys on valid ice in every training year. The term also grows with the number of off-ice buoys, so it still ranks infeasible genotypes and guides the search towards deployable placements.

NSGA-II uses Deb's constrained domination [34]: a feasible solution dominates every infeasible one, the smaller violation wins between two infeasible solutions, and standard dominance (f_1 maximised, f_2 minimised) applies between feasible solutions. The reported front therefore contains only arrays that are on valid ice and meet the DKA geometric requirements, and the violation acts as a search gradient towards feasibility, not as a price that a solution can pay.

2.2.3.6 Ship Operating Cost Objective (f_2)

The second objective minimises the financial operating cost of deploying the array, calculated from the vessel transit route (edge-tracking leg and deployment tour; see the Genotype-to-Phenotype Mapping and Ship Routing sections):

$$f_2(\boldsymbol{z}) = C(\boldsymbol{z}) = \frac{D_{\text{route}(\boldsymbol{z})}}{v_{\text{ship}}} \times \frac{R_{\text{daily}}}{24} \tag{17}$$

where $D_{\text{route}} = D_{\text{edge}} + D_{\text{tour}}$ is the total transit distance from the $w = 0$ ice-edge contact point at the eastern ROI boundary (the anchor line), westward along the edge to the anchor waypoint, and through all buoy deployment waypoints; the open-water approach transit is excluded. $v_{\text{ship}} = 15$ km/h (approx. 8 knots) is a typical vessel transit speed for the *SA Agulhas II* in ice, and $R_{\text{daily}} = \$48,500$ is the approximate daily running cost of the vessel.

2.2.4 Robust Objective Function

The objectives $f_1(\boldsymbol{z})$ and $f_2(\boldsymbol{z})$ defined above are single-year quantities: the genotype $\boldsymbol{z}$ is year-independent, but the phenotype it decodes in year ω, and hence the trajectories, route, and resulting objective values, depend on that year's realised ice conditions. To prevent optimisation for any single year, the 39 training years are treated as samples from the underlying probability distribution of SO ice conditions, and each objective is optimised in expectation over that distribution, estimated as the ensemble mean across the training years.

$$f_i^{\text{rob}(\boldsymbol{z})} = \frac{1}{N_{\text{train}}} \sum_{\omega \in \text{ Train}} f_i(\boldsymbol{z}, \omega), \quad i \in \{1, 2\} \tag{18}$$

The pair $\left(f_1^{\text{rob}}, f_2^{\text{rob}}\right)$ constitutes the two objectives on which NSGA-II searches. This formulation prevents overfitting to specific years and produces strategies that perform well across the climatological distribution.

2.3 Trajectory Simulation

Buoy trajectories are integrated forward using fourth-order Runge-Kutta (RK4) with stochastic diffusion. Integration starts at $t = 0$ on 1 August, with all trajectory forcing drawn from the planned deployment window of 1–14 August. The trajectory model combines deterministic fourth-order Runge-Kutta advection with a stochastic diffusion term representing unresolved sub-grid kinematics [35]. Over each integration time step Δt, the position of each buoy $i \in \{1, ..., n_B\}$ is advanced by:

$$\boldsymbol{r}_i(t + \Delta t) = \boldsymbol{r}_i(t) + \Delta \boldsymbol{r}_{\text{RK4}(\boldsymbol{r}_i(t), t, \Delta t)} + \sqrt{2K\Delta t}\boldsymbol{\xi}_i(t), \tag{19}$$

where $\boldsymbol{r}_i(t) = (x_i(t), y_i(t))^T$ is the horizontal position vector in EASE-Grid South coordinates, $\Delta \boldsymbol{r}_{\text{RK4}}$ is the displacement increment from the classical four-stage RK4 scheme applied to the sea-ice velocity field $\boldsymbol{u}(\boldsymbol{r}, t)$ obtained via spatial bilinear and temporal linear interpolation of the daily gridded motion product, K is the isotropic diffusion coefficient, and $\boldsymbol{\xi}_i(t) \sim \mathcal{N}(\boldsymbol{0}, \boldsymbol{I}_2)$ is a bivariate standard normal variate yielding an isotropic perturbation with standard deviation $\sigma = \sqrt{2K\Delta t}$. The numerical and physical parameters governing the trajectory integration are summarised in Table 5 below.

Table 5 Numerical and physical parameters for Lagrangian trajectory simulation.

Parameter	Value	Description
Time step (Δt)	3 h	RK4 integration step resolving diurnal velocity variations
Simulation duration	14 days	Observational window matching typical Antarctic buoy lifespan
Diffusion coefficient (K)	50 m^2/s	Sub-grid stochastic diffusion [35]
Boundary handling	Last-valid-position	Halts advection if trajectory exits valid velocity support

2.4 Ship Routing

Costing begins at the $w = 0$ point where the ice-edge intersects with the eastern ROI boundary (the anchor line $x = 64$ km). From here the vessel tracks the visible edge westward to the anchor waypoint selected by gene w, then begins buoy deployment. The deployment tour from the anchor waypoint through the n_B buoy positions is modelled as an open TSP with a fixed start (the anchor) and end (the last buoy

visited); the open-water approach transit to the deployment theatre is excluded from the comparison. Given the small problem size (i.e. a small number of buoys), a composite heuristic provides adequate accuracy for this implementation:

1. The routing uses a fixed start where the first buoy visited is the one nearest the anchor waypoint.
2. The tour is chained greedily from that first buoy.
3. The tour is improved by swapping edge pairs if the swap reduces distance, keeping the first buoy fixed.

This heuristic provides a computationally efficient approximation of deployment transit distance suitable for repeated evaluation within the GA loop. Once the vessel has entered the ice, it remains in the ice for the full deployment route, as the high dynamism of the MIZ offers no guarantee of a clear path back to the edge, so no open-water re-entry legs are modelled. Non-genotype baselines (described in Section 2.7) used for comparison are costed with the same tour model starting from the $w = 0$ contact point (no edge-tracking leg), so all strategies share the same operational cost basis.

2.5 NSGA-II Configuration and Pipeline Implementation

This bi-objective optimisation problem is solved using the Non-dominated Sorting Genetic Algorithm II (NSGA-II) [34]. The algorithm was selected for several methodological reasons. The deployment design balances scientific observation coverage ($f_1 \in [0, 1]$, dimensionless) against vessel charter cost (f_2, monetary expenditure in USD). These objectives possess fundamentally different units and conflicting spatial requirements. Rather than combining them into a single scalar fitness using arbitrary weights or a penalty multiplier, which would collapse the search to a single subjective compromise, NSGA-II directly approximates the entire Pareto-optimal frontier. This results in a spectrum of non-dominated strategies across varying budgets. Secondly, the algorithm's μ (parent population size) + λ (offspring population size), elitist selection mechanism ensures that high-performing trade-offs discovered in earlier generations are preserved against genetic drift, while crowding-distance niching maintains an even spread of candidate solutions across the Pareto front without requiring problem-dependent sharing radius parameters (σ_{share}). Constraints enter the selection directly rather than as prices where the geometric and operational validity factors are aggregated into a single violation measure, and candidates are ranked by Deb's constrained domination (feasible before infeasible, infeasible by smaller violation) so that an undeployable geometry cannot reach the front merely by being cheap (Section 2.2.3). Thirdly, the objective space is non-differentiable and multimodal where sharp transitions arise from the geometric cluster validity penalties (v_{init}, v_{shape}, v_{drift} which are developed as piece-wise functions), the on-ice constraint at the edges of the valid deployment cells, and the discrete nearest-neighbour/2-opt tour reorderings, structures across which evolutionary algorithms operate effectively where gradient-based methods fail. Finally, the 13-dimensional continuous genotype is searched using Simulated Binary Crossover (SBX; η_c) and Polynomial Mutation (PM; η_m), with the angular genes (α_1, θ_1, φ_k, θ_k) treated as periodic, wrapped in $[0, 2\pi]$ rather than clamped at artificial bounds, ensuring continuous angular search across the $0/2\pi$ wrap point.

2.5.1 Software Architecture and Pipeline Orchestration

Evaluating a candidate genotype across the 39-year climatological training ensemble requires decoding the feature-relative coordinates against each year's realised 1 August ice edge, simulating n_B buoy trajectories via 4th-order Runge-Kutta advection with bilinear velocity interpolation and sub-grid diffusion, and solving a fixed-start and end TSP. To execute this computational workload efficiently while maintaining strict end-to-end reproducibility, the framework is implemented as an automated pipeline in a Python–Julia hybrid architecture:

- All computationally intensive simulation kernels, feature decoders, TSP tour heuristics, and the NSGA-II evolutionary search are implemented in multi-threaded Julia. Relative to initial Python prototypes, this implementation reduces runtimes by approximately three orders of magnitude.
- A Python driver coordinates run configuration profiles, data bundle preparation, knee-point selection via a normalised-product rule on the Pareto front, publication figure generation and downstream cross-product transfer validation.

- To prevent entrapment in local basins of the 13-dimensional search space (representing the feature-relative genotype encoding of three clusters of three buoys), the driver executes 30 independent runs with distinct pseudo-random seeds. An anytime external archive continuously tracks all non-dominated solutions discovered throughout each run, rejecting candidates that are dominated by, or duplicate in objective space, a solution it already holds. The individual seed archives are subsequently merged into a master Pareto front via global non-dominated sorting.
- The dominated hypervolume of each seed's current non-dominated front is evaluated at each generation against a fixed reference corner, and drives both convergence diagnosis and the stagnation response described below. Following the GA run, a short local search (a memetic refinement step) adjusts genes one or two at a time around the front members to check for improvements the GA missed.

2.5.2 Stagnation Response: Archive-Guided Immigrants and Early Stopping

Each seed monitors its own progress to assess whether it has stopped improving. After at least $g_{\min}$ generations, a seed is said to be stagnant when its relative hypervolume gain over the last W generations is below $\varepsilon_{\mathrm{HV}}$:

$$\frac{H_g - H_{g-W}}{H_{g-W}} < \varepsilon_{\mathrm{HV}}, \tag{20}$$

where H_g is the hypervolume of the seed's non-dominated front at generation g. At stagnation, the seed does not stop. It replaces the worst quarter of its population (most dominated first, ties broken by smallest crowding distance) with immigrants. The immigrants are evaluated on all training years, offered to the anytime archive, and then compete under the usual constrained selection. Each immigrant is a copy of a random archive member[2], changed by the offspring polynomial mutation (index η_m, per-gene probability $\frac{1}{n}$, angular genes wrapped), so one gene changes. Immigrants thus probe the neighbourhoods of known trade-offs, including front members that selection has crowded out. A seed gets at most N_{inj} injections, each followed by a full window of W generations before the next stagnation test. The seed stops at the first stagnation after its last injection, so N_{gen} is only a ceiling. The anytime archive accepts only non-dominated additions, so an injection cannot degrade the reported front.

The end-to-end robust evaluation and evolutionary optimisation procedure is formalised in Algorithm 1.

[2]In a paired test (population 200, 10 seeds, same master seed), archive-guided and uniform random immigrants gave the same pooled hypervolume (within 0.06%), and the archive-guided variant used about 2% fewer evaluations.

Algorithm 1 Robust feature-relative array optimisation and climatological evaluation loop.

Input: Climatological training ensemble Ω_{train}; population size N_{pop}; generation ceiling N_{gen}; independent random seeds S; crossover distribution index η_c; mutation distribution index η_m; stagnation window W, tolerance ε_{HV} and minimum generations $g_{\min}$; injection budget N_{inj}.
Output: Master Pareto-optimal front $\mathcal{P}^*$ of robust feature-relative genotypes $\boldsymbol{z}^*$.

for each independent random seed $s \in \{1, ..., S\}$ **do**
  Initialise population $\mathcal{P}_0$ of N_{pop} genotypes; initialise anytime archive $\mathcal{A}_s \leftarrow \varnothing$
  for generation $g = 0$ **to** N_{gen} **do**
    for each candidate genotype $\boldsymbol{z} \in \mathcal{P}_g$ **do**
      for each climatological training scenario $\omega \in \Omega_{\text{train}}$ **do**
        Decode: Map $\boldsymbol{z}$ to candidate buoy coordinates $\boldsymbol{P}$ relative to realised ice edge $\mathcal{E}_\omega$
        On-ice test: Count the buoys n_{off} that fall outside the valid deployment cells $\mathcal{M}_\omega$ (no repair)
        Route: Solve TSP from entry waypoint $\boldsymbol{g}_{\text{entry}}$ through the decoded buoys via NN + 2-opt $\leftarrow f_2(\boldsymbol{z}, \omega)$
        Simulate: Integrate buoy trajectories $\boldsymbol{r}_{i(t)}$ via RK4 advection with stochastic diffusion
        Score: Evaluate penalised coverage $f_1(\boldsymbol{z}, \omega) = J_{\text{cov}} \times v_{\text{cluster}} \times v_{\text{inter}} \times v_{\text{deploy}} \times v_{\text{ice}}$ (maximised) and violation $v(\boldsymbol{z}, \omega)$
      end for
      Aggregate robust objectives and violation: $f_i^{\text{rob}(\boldsymbol{z})} \leftarrow \frac{1}{\lvert}\Omega_{\text{train}}\rvert \sum_\omega f_{i(\boldsymbol{z},\omega)}$ for $i \in \{1, 2\}$, and $v^{\text{rob}} \leftarrow \frac{1}{\lvert}\Omega_{\text{train}}\rvert \sum_\omega v$
    end for
    Update anytime archive: $\mathcal{A}_s \leftarrow \text{NonDominatedSort}(\mathcal{A}_s \cup \mathcal{P}_g)$
    Generate offspring $\mathcal{Q}_g$ via SBX crossover (with modular angular wrapping) and polynomial mutation
    Evaluate $\mathcal{Q}_g$ across Ω_{train}; select next population $\mathcal{P}_{g+1}$ via **constrained** non-dominated sorting (feasible $\succ$ infeasible; infeasible ranked by v^{rob}) and crowding distance
    if $g \geq g_{\min}$ **and** relative hypervolume gain over the last W generations $< \varepsilon_{\text{HV}}$ **then**
      if fewer than N_{inj} injections used **then** replace the worst 25% of $\mathcal{P}_{g+1}$ with mutated copies of random members of $\mathcal{A}_s$ (archive-guided immigrants); evaluate them and add them to $\mathcal{A}_s$
      else stop this seed (early stop)
  end for
end for
Pool archives across all seeds $\mathcal{A}_{\text{all}} = \cup_{s=1}^{S} \mathcal{A}_s$ and extract master front $\mathcal{P}^* \leftarrow \text{NonDominatedSort}(\mathcal{A}_{\text{all}})$
return $\mathcal{P}^*$

The optimisation produces a Pareto front of non-dominated solutions representing optimal trade-offs between coverage and cost. Because the front contains only feasible arrays, on valid ice and DKA-valid (see Section 2.2.3), every member is a candidate strategy in its own right. The full set of algorithm hyperparameters and simulation settings for the publication-scale experiment is detailed in Table 6 (Section 3). In practice, the specific solution chosen for implementation is likely to be determined by the available budget that can be allocated to the deployment. That is, for a given budget, the solution on the Pareto front with the highest coverage is likely to be selected. However, the knee point of the Pareto front is also a natural candidate for selection, as it marks the beginning of the region of diminishing returns; the transition beyond which each additional unit of coverage is bought at a proportionally higher cost. In this work, the knee point is taken as the reference for the comparisons that follow and is referred to as the "proposed strategy". The proposed strategy is selected by a normalised-product rule. For each front member i, the 39-year mean penalised coverage $f_{1,i}$ and the mean ship cost C_i are min–max normalised across the front, with cost reversed so that the cheapest member scores one:

$$\hat{f}_{1,i} = \frac{f_{1,i} - \min_j f_{1,j}}{\max_j f_{1,j} - \min_j f_{1,j}}, \quad \hat{C}_i = \frac{\max_j C_j - C_i}{\max_j C_j - \min_j C_j}. \tag{21}$$

The proposed strategy is the member that maximises $\hat{f}_{1,i}\,\hat{C}_i$. Both extremes of the front score zero, so the rule selects a balanced compromise between the two objectives, near the bend of the front. Every front member is optimal, and other knee definitions are equally valid; this one serves only as a fixed reference for the comparisons that follow.

2.6 Blind Validation Protocol

The robust objective function (Section 2.2.4) optimises in expectation over the 39 training years. To establish the performance of the strategy on unseen data, and hence to indicate its generalisability to unseen ice-edge conditions, the resulting strategy undergoes blind validation after the conclusion of Algorithm 1, which optimises using only the 1979–2017 data.

The proposed genotype is then applied to all 7 test years (2018–2024) where feature-relative genes are mapped to physical coordinates using each year's ice edge; the trajectories are then simulated through the corresponding velocity field, and the coverage and cost metrics are evaluated. The years 2018–2024 were selected for use as the blind validation years for two reasons: first, they are the most recent years for which the PP drift product is available and thus represent the most up-to-date climatological conditions, and second, they include a range of ice-edge conditions ranging between extreme low ice years (2018, 2022) and extreme high ice years (2020, 2023), providing a robust test of the strategy's generalisability.

2.7 Baseline Comparisons

Following optimisation and knee selection of the proposed strategy (Section 2.6), its coverage–cost performance is also benchmarked against four baseline strategies that provide context for performance evaluation:

- First, against random selections of valid deployment cells that are not constrained to satisfy the DKA cluster geometry; the strongest of 50 draws by multi-year mean coverage is reported.
- Second, against a strategy optimised for 2023 (an illustrative, specific test year), then applied to all years.
- Third, against a regular rectangular grid deployment.
- Fourth, against a 3×3 arc fan emanating from the lower-right ROI corner, with the outer ring of buoys adjacent to the ice edge. This approximates a deployment style used in the 2022 SCALE Winter Expedition during the same seasonal window, and is therefore a direct historical benchmark.

2.8 Cross-Product Drift Transfer Protocol

While the blind validation of the proposed strategy described in Section 2.6 is necessary, good performance in blind years is still insufficient to establish that the optimised strategy generalises: the optimiser could still exploit PP-specific drift structure, spatial support, or preprocessing to arrive at effective solutions. To test this possibility, the PP-trained publication genotype is held fixed and, for each blind year, decoded in the feature frame supplied by two alternative observational drift products (DPGSIV and OSI-405-c), then simulated through the corresponding velocity field from these products. Neither external product is used to train or tune the genetic algorithm or its resultant strategy. The comparison simply asks whether the PP-derived decision rule remains useful when both the feature location (ice edge) and the trajectory forcing are derived from external, alternative processing pipelines.

2.8.1 Frozen-transfer protocol

To achieve this, the knee strategy from the PP-trained optimisation is frozen and applied to the alternative drift products (DPGSIV and OSI-405-c) in each of the 7 blind years. Feature-relative decoding followed the ice-edge representation defined earlier. The first cluster's along-edge gene selected a normalised arc-length position (w) along the 1 August ice edge contour line within the deployment sector. Its distance gene (d_1) then displaced Cluster 1 from that contour point along the frozen heading α_1. The remaining clusters were placed relative to the preceding cluster using the frozen relative-distance (d_k) and bearing (φ_k) genes.

Neither external drift record includes a concentration-derived ice edge matching the PP preprocessing. The northern boundary of valid drift support was therefore treated as an operational proxy feature edge. For each projected grid column within the drift domain, the northernmost supported cell on 1 August was extracted, smoothed, ordered west to east, and resampled at uniform arc length. The deployment ROI, the valid deployment cells, and the evaluation grid were then constructed relative to this product-specific boundary with the same rules as for PP. The ROI was anchored on the line $x = 64$ km, and valid cells were restricted to supported cells on the pack side of the proxy edge and at least 10 km from it.

2.8.2 Validation drift products

The DPGSIV record contains daily 24-hour sea-ice displacement vectors derived from AMSR2 on a 60 km Southern Hemisphere grid [33]. Sixteen daily field records (from 1–16 August each year) were used to provide a 14-day integration window with a two-day buffer. In preprocessing, displacement endpoints were projected from the provider's stereographic frame into the PP simulator's EASE-Grid South (Lambert azimuthal equal-area) frame, converted to metres per second and assigned to the common 10 km canonical sector by bounded nearest-neighbour regridding with a 90 km support radius; sentinel gaps were retained rather than filled.

OSI-405-c is the Southern Hemisphere low-resolution merged OSI SAF drift product on a 62.5 km polar stereographic grid [32]. The validation uses the archived OSI-405-c files covering 2018–2024. Daily files describe nominally 48-hour displacements. Sixteen end-date files from 1–16 August were downloaded for each year. For each file the start and end geographic coordinates were projected separately into the PP frame, the component displacements were divided by the actual interval between each cell's start and end observations (nominally 48 h) to give mean velocities in metres per second, and vectors flagged as invalid by the product's status flag were discarded before bounded nearest-neighbour regridding onto the same 10 km grid with a 95 km support radius. It is worth noting that these validation datasets are not completely sensor-independent: DPGSIV and OSI-405-c share raw satellite observations (notably AMSR2 and SSMIS) with the multi-sensor Polar Pathfinder product. However, their motion extraction algorithms (single-sensor MCC and multi-sensor CMCC, respectively, without wind blending), spatial grids, temporal intervals, and operational masking are completely distinct, providing an effective test of whether the optimised strategy overfits to PP-specific processing artefacts.

Temporal handling is common to all three products: no temporal interpolation is applied during preprocessing, and instead each product's daily fields are linearly interpolated in time inside the RK4 integrator, which advances trajectories in 3-hour steps.

2.8.3 Eligibility and reference strategies

All nine decoded initial positions must lie in cells where the external product supplies a velocity (supported cells), so that every trajectory starts inside observed drift. Unlike PP, whose valid-velocity mask is complete over the drift domain, the external products have gaps in space and time, because sensor swaths and masking leave parts of the domain without observed vectors. After integration, trajectory support was therefore calculated as the fraction of all simulated positions at which the product could supply a velocity. A buoy can leave supported cells in any direction. Loss of support is most likely for buoys that start near the product's proxy edge, because that edge is the northern limit of its drift field and the mean drift in this sector has a northward component. Where support is lost the simulator holds the last valid position, so an unsupported position is a placeholder rather than an observed displacement; were such positions to dominate a trajectory, the coverage and cost metrics would describe the holding behaviour rather than real ice motion. Coverage and cost were therefore accepted only when the pooled trajectory support reached at least 75%, guaranteeing that at least three-quarters of the simulated positions were advected by genuinely observed velocities. The threshold tolerates up to a quarter of the integration being unsupported, accommodating edge-adjacent drift and the coarse 90–95 km support radius without admitting years whose drift is mostly unresolved. Years failing the gate were retained in the audit with an explicit status and excluded from performance means rather than imputed as zero, since a zero would falsely assert poor performance and bias the cross-product comparison.

In this way, the frozen feature-relative design was compared with a deterministic grid, 50 independently generated random deployments per year, and the historical fixed-coordinate deployment. Grid and random positions were generated from the supported product-relative deployment region. The fixed-coordinate case is a diagnostic of direct GPS transfer and was scored only when it met the same support rules. Paired PP–DPGSIV–OSI-405 inference uses the intersection of complete years so that every line in the comparison represents the same deployment year.

3 Computational Experiments

To evaluate the proposed deployment strategy, a series of computational experiments was conducted. The experiments were designed to assess the performance of the optimised deployment strategy against baseline strategies, as well as to evaluate its robustness and generalisability across different years and alternative drift products using the methodology developed in the previous sections. The results presented in Section 4 are derived from the experiment protocol described below.

3.1 Experimental Protocol

All stochastic results in this paper follow a single experimental protocol, configured according to Table 6:

Table 6 Array, NSGA-II and simulation configuration for the publication-scale run.

Parameter	Value	Role
Clusters n_{C}	3	Triads per array
Buoys per cluster	3	$n_B = 9$ buoys per array
Genotype length n	13	$n = 4n_{\mathrm{C}} + 1$
Population size	300	Per-seed population
Generation ceiling N_{gen}	400	Per-seed upper limit; 28 seeds stopped early at 228–388
Independent seeds	30	Multi-start; pooled master Pareto front
Base random seed	20261004	Reproducibility
Stagnation window W / tolerance $\varepsilon_{\mathrm{HV}}$	30 / 10^{-3}	Relative hypervolume gain test
Minimum generations $g_{\min}$	80	Before the stagnation test activates
Diversity injections N_{inj}	3 (25% of population)	Archive-guided immigrants per seed
Simulated Binary Crossover index η_c	10	Crossover operator
Polynomial Mutation index η_m	12	Mutation, probability $p_m = \frac{1}{n}$
Crossover probability	0.9	–
Drift duration	14 days	Trajectory horizon
RK4 time step	3 h	Trajectory integration
Diffusion coefficient K	50 m^2/s	Stochastic sub-grid forcing

First, the NSGA-II is configured as in Table 6, with a population of 300 candidates, repeated for 30 independent random seeds. Each seed runs until its stagnation budget is exhausted (Section 2.5.2), with 400 generations as a ceiling. 28 of the 30 seeds used their three archive-guided injections and stopped between generations 228 and 388, while the remaining two were still improving after two injections when they reached the ceiling (median stopping generation 284), for a total of 2.69×10^6 robust evaluations. Every candidate is scored across all 39 training years (expected-value objectives). The anytime archives from each seed are pooled into a master Pareto front and the knee point is selected.[3] The frozen knee genotype is decoded against each test year's realised ice edge and simulated without further tuning (7 unseen years, 2018–2024). The performance of the selected strategy is compared against the random, fixed-coordinate (2023-optimised), grid, and fan deployments evaluated under identical simulator settings.

The three operator parameters in Table 6, Simulated Binary Crossover (SBX), Polynomial Mutation (PM), and crossover probability, are chosen to follow the canonical settings of K. Deb, A. Pratap, S. Agarwal, and T. Meyarivan [34]. They are also linked to the structure of the $n = 13$ gene genotype

[3]Configuration experiments showed that pooling independent seeds at a moderate per-seed budget reproduces the front quality of longer single-basin runs at equal total budget, so independent seed diversity is preferred over longer single-basin runs.

defined in Section 2.2.1 ($n = 4n_{\mathrm{C}} + 1$ for three clusters, i.e. five genes for the anchor cluster and four per chain cluster). SBX distribution index $\eta_c = 10$ sits at the explorative end of the standard 10–20 range. SBX draws offspring from a bimodal beta distribution whose spread falls as $\frac{1}{\eta_c+1}$, so moderate values concentrate children near their parents while still sampling the interval between them. The lower $\eta_c = 10$ favours a broad search through the space within the per-seed generation budget, and any residual sensitivity to this choice is absorbed by the 30-seed pooling described above. PM, with index $\eta_m = 12$ and per-gene probability $p_m = \frac{1}{n}$, perturbs on average exactly one gene per offspring. This constrains mutations to a single gene per offspring, preventing the simultaneous mutation of multiple genes, which would likely violate the geometric constraints required for cluster validity. The index $\eta_m = 12$ then sets a moderate perturbation magnitude: large enough for a mutated gene to move a substantial fraction of its normalised range and discover new bearings or separations, yet bounded enough to act as a local refinement rather than white noise. The crossover probability $p_c = 0.9$ is the default of the original NSGA-II formulation [34]: recombination remains dominant so that beneficial gene linkages propagate across generations, while the one-gene mutation rate supplies the diversity that prevents premature fixation. Together these settings place the search within NSGA-II's standard operating envelope, with independent-seed diversity rather than operator fine-tuning providing the final front-quality guarantee.

4 Results

4.1 Pareto Front and Knee Selection

The robust multi-seed optimisation over 39 training years produces a master Pareto front of non-dominated, feasible solutions shown in Fig. 3 below, spanning a 39-year mean coverage of 0.818–0.932 at \$20.6k–\$47.9k. Because deployability is a hard constraint and the decoder applies no repair, every member of the front places all nine buoys on valid ice cells in all 39 training years as decoded, which was confirmed by re-decoding the full front against each training year. The knee point, selected as the proposed strategy, achieves a balanced trade-off at ~\$28.8k, with a mean penalised coverage of 0.898 over the 39 training years.

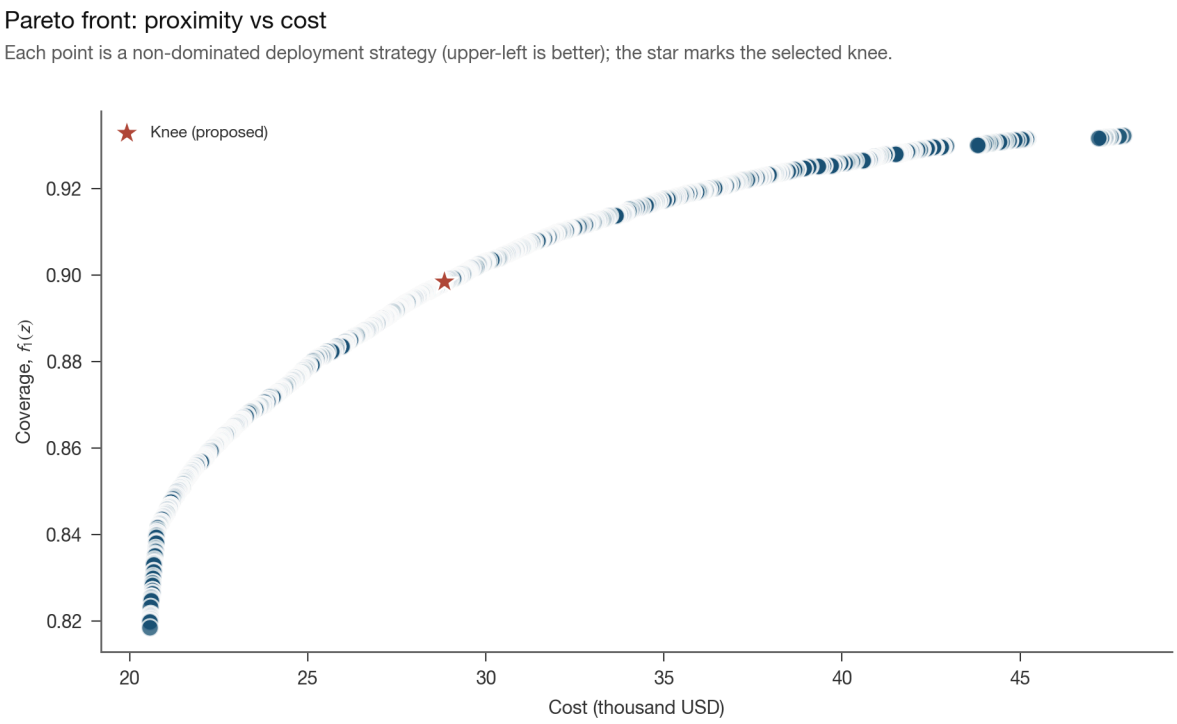


Fig. 3 Pareto front showing non-dominated solutions from robust multi-seed optimisation over 39 training years (300 individuals, 30 seeds, stopped at generations 228–400). The knee point (red star, ~$28.8k at a 39-year mean coverage of 0.898) is selected as the proposed strategy.

4.1.1 Convergence and Local Refinement

Two mechanisms were used to assess the convergence of the NSGA-II optimiser: per-generation hypervolume tracking (the coverage × cost area dominated by the front) and a local search that tests whether small changes to the genes of the master-front solutions can still improve them. The hypervolume curves shown in Fig. 4 demonstrate convergence across the 30 independent seeds. Every seed stagnated at least twice (Section 2.5.2) and received archive-guided injections, each of which extended its search by at least a further 30 generations; 28 seeds exhausted all three injections and stopped between generations 228 and 388, and the two seeds that reached the 400-generation ceiling finished mid-range among the seed finals (1.608 and 1.611×10^6), so the ceiling did not truncate a superior search. Once the front's dominated volume stops growing despite these injections, additional generations of the same search basin do not improve solution quality, and the search is better served by more independent seeds.

Additionally, the local search took 150 evenly spaced members of the pooled master front and changed their genes one at a time, and four interacting gene pairs jointly, by ±15% of each gene's range and then by ±7.5%, keeping a change only if it dominated the original solution. This changed the dominated hypervolume by less than 0.0001%, confirming that the individual-seed searches had already saturated before their stagnation budgets ran out and that the non-dominated solutions had already been achieved.

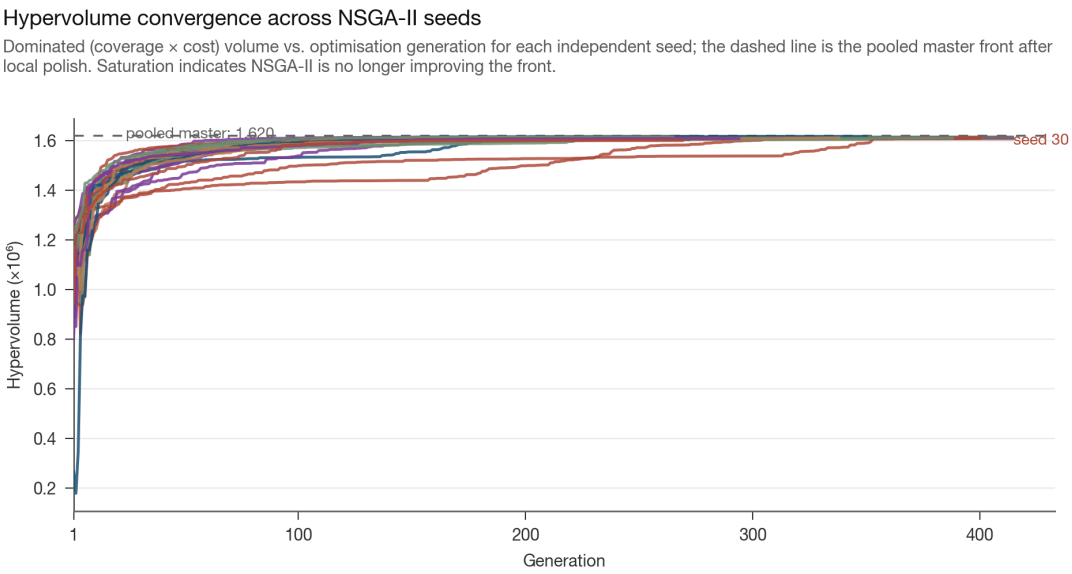


Fig. 4 Hypervolume convergence across the 30 independent seeds. Each line is the dominated coverage × cost volume of the seed's running non-dominated front versus optimisation generation, ending at the generation where the seed's stagnation budget was exhausted or at the 400-generation ceiling; the dashed reference is the pooled master front after the local search. The flattening curves indicate the search has saturated and further generations of a single seed yield no improvement.

4.1.2 Proposed Strategy Deployment

The knee-point strategy selected from the Pareto front in Fig. 3 deploys three clusters of three buoys each (nine in total) in the triangular configurations shown in Fig. 5 below. The figure decodes the genotype for August 2022 and August 2023, illustrating the robustness of the genotype to differing ice-edge locations and contours. The genotype reproduces the same edge-relative construction in both years, with the $w = 0$ contact point on the anchor line lying 86.5 km further south in 2023 than in 2022, and because every cluster is chained from it, the whole array translates southward with it. Cluster 1 is placed 16–18 km from the edge in both years. The distances of Clusters 2 and 3 from the edge differ between the years (79 and 23 km in 2022, 124 and 74 km in 2023) because the edge west of the anchor line has a different shape in each year.

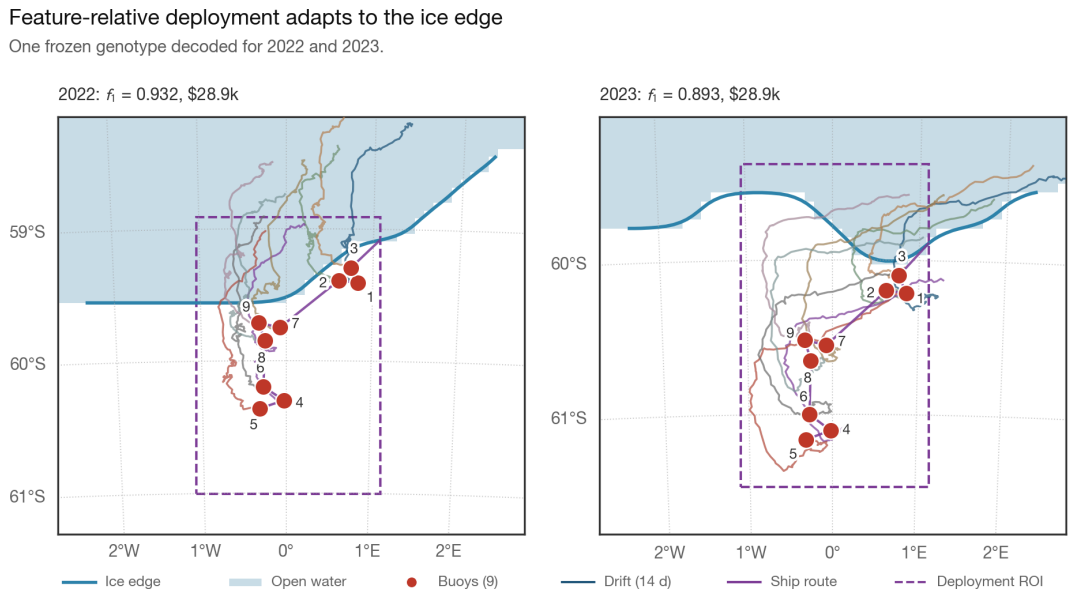


Fig. 5 Proposed strategy deployment for two held-out years. One frozen feature-relative genotype is decoded against the 2022 (left) and 2023 (right) ice edges, with deployed positions (markers), 14-day simulated drift trajectories (tracks), and the optimised ship route (solid violet) shown relative to that year's ice edge and pack ice.

Table 7 that follows presents this proposed strategy in terms of the decoded physical parameters of the three clusters. The table shows the anchor cluster's position along the ice edge (w), the distance of its centroid from the anchor point (d_1), and the heading of that displacement (α_1). The remaining clusters are defined relative to their predecessor by range (d_k) and bearing (φ_k). The triangle heading angles (θ_k) and side lengths (s_k) are also shown for each cluster.

Table 7 Decoded physical parameters for the optimal knee deployment strategy.

Cluster	Parameter	Decoded Value	Description
Cluster 1	w	0.000	Anchor exactly at the eastern ROI boundary ($w = 0$ contact point)
	d_1	36.5 km	Distance of the Cluster 1 centroid from the anchor point
	α_1	214.9°	Heading of the Cluster 1 displacement (clockwise from the grid $+y$ axis)
	θ_1	128.9°	Triangle orientation (clockwise from the grid $+y$ axis)
	s_1	13.3 km	Triangle side length
Cluster 2	d_2	112.8 km	Distance from Cluster 1 centroid
	φ_2	208.9°	Heading from Cluster 1 centroid (clockwise from the grid $+y$ axis)
	θ_2	98.4°	Triangle orientation (clockwise from the grid $+y$ axis)
	s_2	17.8 km	Triangle side length
Cluster 3	d_3	55.5 km	Distance from Cluster 2 centroid
	φ_3	359.1°	Heading from Cluster 2 centroid (clockwise from the grid $+y$ axis)
	θ_3	74.2°	Triangle orientation (clockwise from the grid $+y$ axis)
	s_3	14.8 km	Triangle side length

Three features of the decoded strategy reflect the operational cost model and the deployability constraint directly. The placement gene sits at $w = 0$: the optimiser anchors Cluster 1 exactly at the eastern ROI boundary, so there is no westward edge-tracking leg and the vessel turns into the pack immediately upon reaching the ice edge. The Cluster 1 heading, $\alpha_1 \approx 215°$, points south-south-west into the pack, so the $d_1 = 36.5$ km displacement places the Cluster 1 centroid 29.9 km south and 20.9 km west of the anchor

point. Coverage is then achieved through the chained placement of Clusters 2 and 3 (d_2, φ_2, d_3, φ_3). Cluster 2 is chained 112.8 km on a south-south-westerly bearing $\varphi_2 \approx 209°$, 124 km from the edge (in 2023), and Cluster 3 folds back due north ($\varphi_3 \approx 359°$) by 55.5 km, to 74 km from the edge (in 2023), so that the three centroids form a 55–113 km triangle spanning the eastern and central parts of the ROI. Neither chain distance sits at a bound, although d_3 lies close to the 50 km inter-cluster minimum, while the triad side lengths ($s_k = 13.3$–17.8 km) sit in the lower half of the 10–30 km DKA window.[4]

Those decoded parameters convert directly into an operational waypoint schedule, on which the ship operating cost objective f_2 is evaluated. The conversion is anchored on the $w = 0$ contact point defined in Section 2.2.1: the point where the vessel meets the ice edge on the eastern deployment-ROI boundary ($x = 64$ km, near $1°E$), having arrived from Cape Town. Because the placement gene sits at $w = 0$, the anchor coincides with that contact point, so the vessel turns into the pack directly from the $w = 0$ point and runs an open deployment tour over the buoys. The tour order is the one the cost model selects rather than the order in which the genotype numbers the buoys, so the tour runs cluster 1, then cluster 3, then cluster 2, and ends on the southernmost triad. Table 8 gives the resulting schedule for the 2023 example year, a total of 214.5 km (14.3 h at 15 km/h).

Table 8 Decoded 2023 waypoint schedule for the knee-point strategy, converted from the genotype via the $w = 0$ ice-edge contact point at the eastern deployment-ROI boundary. Waypoints follow the ship route shown in Fig. 5 inbound leg and true heading describe the leg arriving at each waypoint from the previous one. The schedule begins at $w = 0$ and excludes the open-water approach, as does the cost model.

WP	Waypoint	Latitude	Longitude	Leg (km)	Heading
0	Route start and edge anchor ($w = 0$, eastern ROI boundary)	59.888°S	1.103°E	–	–
1	Buoy 3 (cluster 1)	60.099°S	0.768°E	29.8	218.3°
2	Buoy 1 (cluster 1)	60.214°S	0.855°E	13.3	159.4°
3	Buoy 2 (cluster 1)	60.196°S	0.624°E	13.3	278.6°
4	Buoy 7 (cluster 3)	60.553°S	0.075°W	55.2	223.8°
5	Buoy 9 (cluster 3)	60.519°S	0.329°W	14.9	285.3°
6	Buoy 8 (cluster 3)	60.652°S	0.259°W	14.9	165.5°
7	Buoy 6 (cluster 2)	61.001°S	0.277°W	37.7	181.4°
8	Buoy 4 (cluster 2)	61.104°S	0.027°W	17.8	130.5°
9	Buoy 5 (cluster 2)	61.164°S	0.325°W	17.8	247.2°

4.2 Blind-Year Validation Against Baselines

4.2.1 Blind Validation Results

The proposed feature-relative strategy was then applied to the unseen test years in the computational experiment. The results of this blind validation are summarised in Table 9 below, which compares the mean and standard deviation of coverage and cost across the training years (1979–2017) and the test years (2018–2024).

Table 9 Blind validation results comparing training and test performance.

Metric	Training (1979–2017)	Testing (2018–2024)	Retention
Coverage, $f_1(\boldsymbol{z})$ (mean ± std)	0.898 ± 0.016	0.893 ± 0.027	99.4%
Cost (mean ± std)	\$28.8k ± \$0.3k	\$28.6k ± \$0.6k	99.3%

[4]These decoded parameters are specific to the knee point; other Pareto-front members decode to different parameter values.

The 99.4% coverage retention in the test years shows that the strategy performs on unseen years almost as well as on its training climatology, with a mean decrease of only 0.005 in f_1. Annual test coverage spans 0.834–0.932, and the decrease comes from a single year, 2018, which has the lowest score (0.834). In 2018 the realised edge is the most atypical of the test years within the deployment region, and the fixed-coordinate baseline also collapses there, to 0.235. West of the anchor line the edge climbs nearly 100 km northward in 2018, leaving the deployed array deeper in the ice than in other years. The other six test years span 0.893–0.932, with a mean of 0.903 ± 0.013 that is slightly above the training mean (100.6% retention). These results support the claim that the feature-relative approach addresses the hindcast-to-forecast problem and that the proposed strategy generalises to unseen years, although edge geometries far outside the typical configuration degrade performance. Test-year cost is stable and slightly below the training mean ($28.6k ± $0.6k against $28.8k ± $0.3k). With the anchor at $w = 0$ the array moves rigidly with the edge, so the costed route is the same ($28.9k) in every year in which no centroid is clipped at the ROI boundary. The cost changes only when clipping alters the geometry, as in 2018 ($27.1k). These performance metrics are visualised in Fig. 6 below.

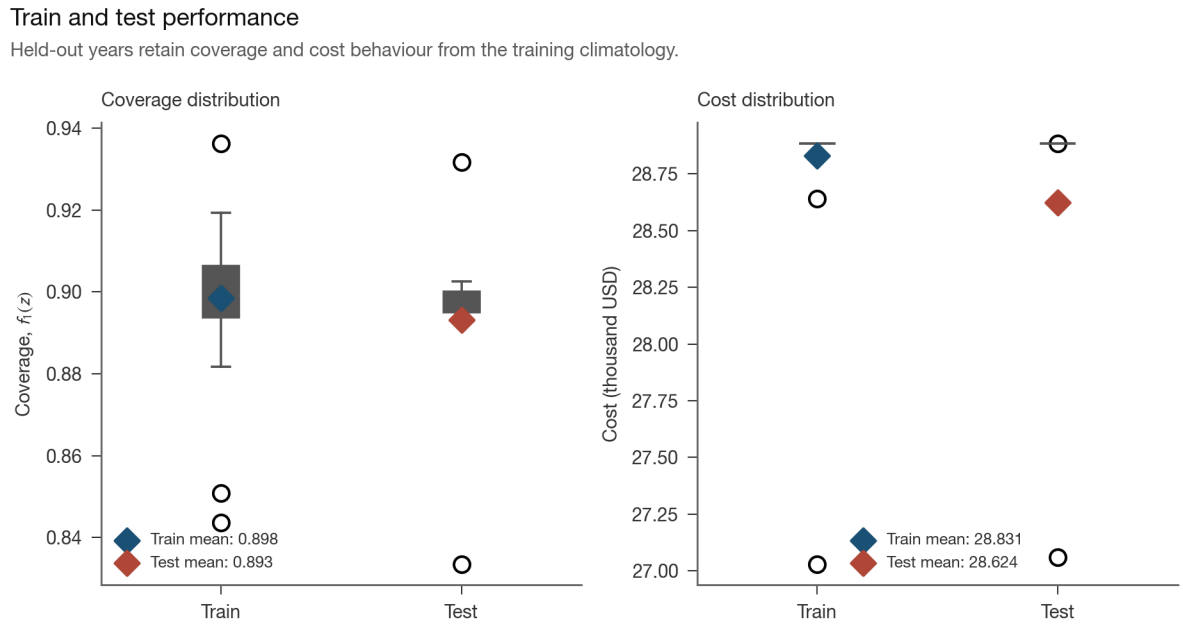


Fig. 6 Training vs. testing boxplots showing coverage and cost distributions across the 39 training and 7 test years; diamonds mark the training (blue) and test (red) means and open circles are outlying years. Test years cluster around the training median (99.4% retention), with 2018 visible as the low test-year outlier; cost is identical in every year except those in which a cluster centroid is clipped at the ROI boundary.

4.2.2 Baseline Comparison

Following the presentation of the blind validation, here the feature-relative strategy is shown to significantly outperform the baselines described in Section 2.7. Performance metrics for the proposed strategy and the four baselines are summarised in Table 10 below, which compares the mean and standard deviation of coverage and cost across the test years (2018–2024).

Table 10 Performance comparison: proposed strategy vs. baselines (mean ± std across test years 2018–2024).

Strategy	Coverage, $f_1(\boldsymbol{z})$	Cost	Improvement
Proposed (feature-relative)	0.893 ± 0.027	\$28.6k ± \$0.6k	–
Fixed-coordinate (2023-opt)	0.518 ± 0.307	\$32.4k ± \$4.7k	−42% coverage
Random (best of 50)	0.402 ± 0.081	\$51.9k ± \$6.6k	−55% coverage
Grid pattern	0.389 ± 0.007	\$49.4k ± \$1.6k	−56% coverage
Fan pattern (2022-style)	0.316 ± 0.013	\$43.3k ± \$2.6k	−65% coverage

The fixed-coordinate baseline illustrates the unreliability of a strategy optimised for a specific year (in this case, 2023): its mean coverage of 0.518 across the test years masks a degradation to 0.24–0.28 in 2018–2021, when the realised ice edge lay far from the 2023-optimised coordinates and its snapped triads collapsed to collinear strings, and a recovery to 0.80–0.92 only in 2022–2024. Even with that partial recovery its mean coverage is 42% below the proposed strategy, with more than eleven times the standard deviation, and it is also 13% more expensive (\$32.4k against \$28.6k); only in its own tuning year, 2023, does it edge the proposed strategy (0.920 against 0.893). The random and grid baselines achieve approximately 45% and 44% of the proposed coverage at 1.81 and 1.72 times the cost, respectively, while the fan baseline (representative of the SCALE 2022 Winter deployment pattern) reaches only 35% of the proposed coverage at 1.51 times the cost. Thus, for the problem presented in this work, the proposed feature-relative strategy outperforms all baselines on usable coverage, achieving 1.7–2.8 times theirs, while also being the cheapest strategy: 12% cheaper than the fixed-coordinate draw, 34% cheaper than the fan, and 42–45% cheaper than the grid and random references. The compared strategies are shown in Fig. 7 below, which illustrates the initial buoy positions and simulated drift tracks for the 2023 test year.

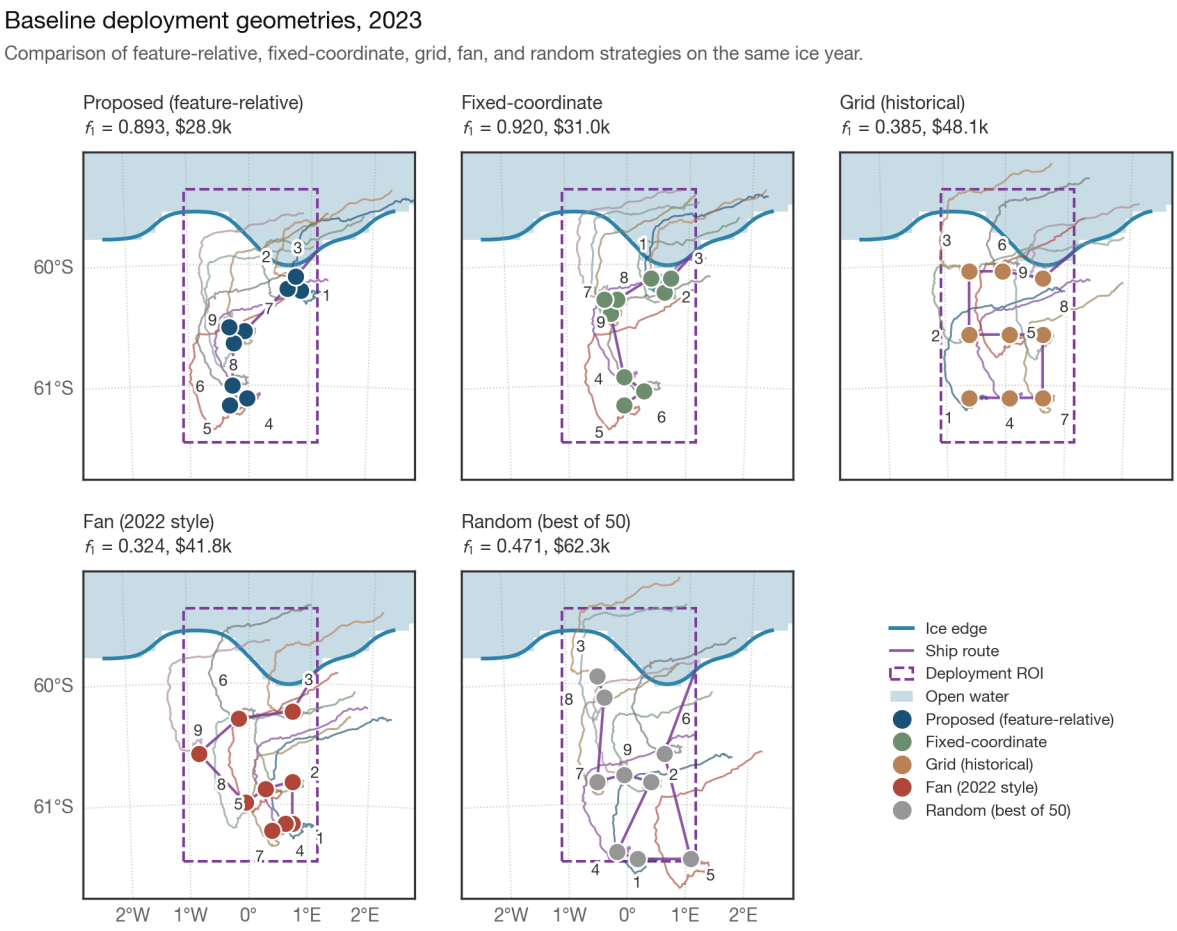


Fig. 7 Example deployment geometries for 2023. Each panel shows initial buoy positions (numbered), simulated 14-day drift tracks, the ice edge, deployment ROI, and optimised ship route for one baseline strategy; the random panel shows the strongest of 50 uniform draws of nine valid ice cells (no DKA cluster constraints). The annotated coverage and cost are those recorded for 2023 in the run's baseline artifact, so they are directly comparable with Table 10.

Here, a comparison between the proposed and fan-style deployments reveals similar-looking drift tracks, sweeping a comparable area, while the proximity scores differ significantly. In the 2023 comparison year the raw proximity metric, from Eq. 4 (i.e. the mean distance from each evaluation cell to the nearest trajectory point, before any penalties), is 23.0 km for the fan and 25.2 km for the proposed strategy. The reported objective, however, Eq. 15, is the penalised coverage $f_1 = J_{\text{cov}} \times v_{\text{cluster}} \times v_{\text{inter}} \times v_{\text{deploy}} \times v_{\text{ice}}$, and it is the penalty factors that separate the strategies. Each fan cluster comprises three buoys laid out along a single radial ray where initial pairwise spacings of 35–104 km violate the 10–30 km deployment window, the cluster shape is exactly collinear (linearity ratio 1.00, against the 0.6 threshold, which drives the shape score to its lowest attainable value), and two of the three centroid pairs sit only 27–28 km apart, below the 50 km inter-cluster minimum required for independent differential kinematic analysis. The fan therefore retains only ≈ 0.36 of its raw spatial score (0.324 reported coverage in 2023, against a raw score of 0.911). The proposed strategy, by contrast, deploys equilateral 13.3–17.8 km triangles with centroids 55–113 km apart, and retains 99% of its raw spatial score (0.893 reported, against a raw score of 0.902).

This penalty structure is deliberate and should not be read as a quirk of the scoring rule. The array exists to support differential kinematic analysis, which requires non-collinear triangular clusters with mesoscale separation between independent groups. The coverage figures in Table 10 therefore measure usable coverage (proximity weighted by the geometric validity of the observing configuration) and under that measure the visual similarity of the drift tracks is immaterial. Notably, the raw spatial term alone only marginally separates the strategies and slightly favours the unconstrained baselines: across the seven test years the grid, random, and fan deployments reach mean raw spatial scores of 0.94, 0.92, and 0.90

against 0.90 for the proposed strategy, because they scatter buoys across the region without regard for cluster geometry. That proximity is largely unusable for differential kinematic analysis at the mesoscale, and removing it is precisely what the penalty factors do; under the reported objective the proposed strategy leads every baseline on coverage at lower cost than any of them.

Fig. 8 below summarises the coverage and cost distributions across the test years for the proposed strategy and the four baselines on a coverage versus cost plot. The proposed strategy (blue) achieves the highest coverage, with variance driven by the seven-year test sample; the fixed-coordinate (green) baseline shows extreme spread, matching the proposed at similar cost only when the ice edge happens to be near its 2023-optimised coordinates, but collapsing away from them in most test years. The grid (orange), random (grey), and 2022-style fan (red) baselines sit far below on coverage.

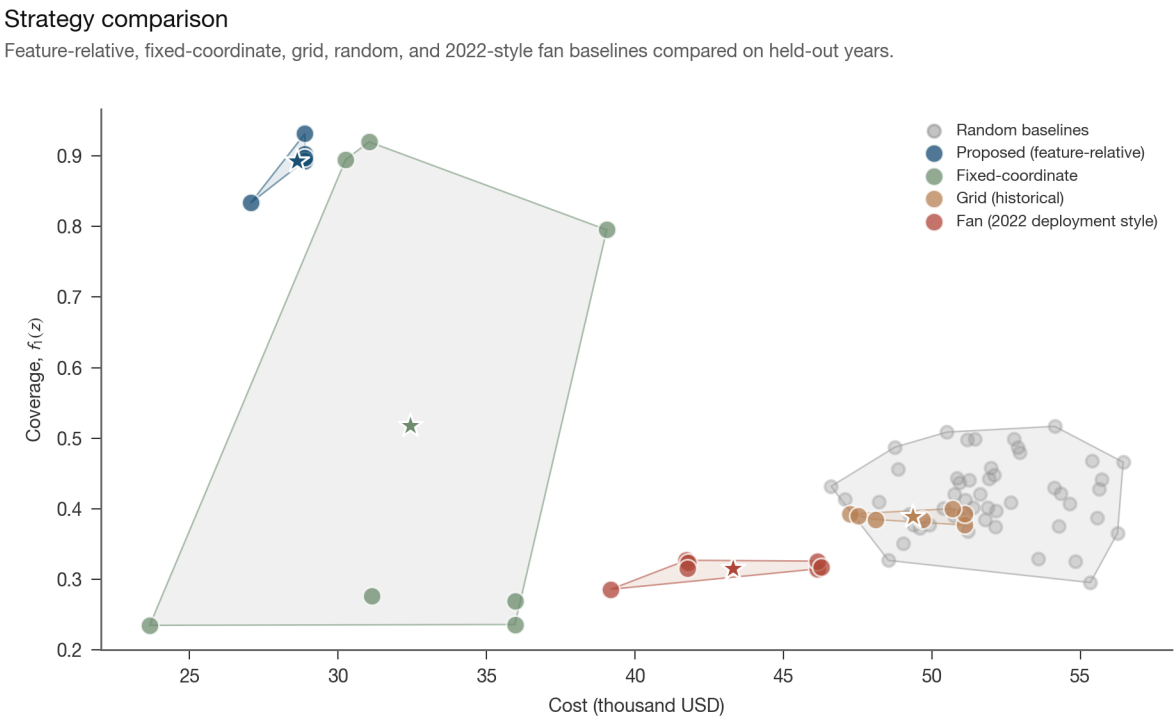


Fig. 8 Strategy comparison showing coverage and cost distributions across test years. The proposed feature-relative strategy (blue) achieves higher coverage with lower variance compared to fixed-coordinate (green), grid (orange), random (grey), and 2022-style fan (red) baselines. Coloured dots are individual test years, shaded polygons are the convex hull of each strategy's points, and stars mark each strategy's mean over the test years; the grey dots are the 50 random draws, each plotted at its own multi-year mean, of which the strongest is reported in Table 10.

4.3 Local Sensitivity and Operational Tolerance

The preceding sections establish that the proposed strategy generalises well to unseen years. This section assesses the sensitivity of the genotype to errors in each gene. To characterise the robustness of the selected strategy and to identify which deployment instructions require the tightest operational control, a local response-surface analysis was performed around the knee-point genotype. Each of the 13 genes was perturbed individually at nine values within a local window, and every perturbed genotype was re-evaluated, with the on-ice constraint active, across the 46-year evaluation ensemble (39 training years plus the 7 test years); the three most sensitive genes were then varied in all three pairwise combinations on 9 by 9 grids to expose interactions. A separate operational test displaced all nine buoy drop positions with isotropic Gaussian errors, using 50 perturbation samples per level and the same 46-year ensemble. This positional test is a proxy for final drop-location error rather than a full model of continuous ship-track deviation.

4.3.1 One-at-a-time gene sensitivity

To quantitatively rank gene sensitivities across the two objectives (penalised coverage in $[0, 1]$ and monetary ship-transit cost), each gene g_i was evaluated across its local perturbation sweep while holding all remaining genes fixed at their baseline knee-point values. The unperturbed baseline under this penalised re-evaluation is $f_{1,0} = 0.898$ at $\text{Cost}_0 = \text{R}475,190 \approx \$28,799$ (the penalised ensemble mean over all 46 evaluated years, 39 training years plus the 7 test years). The maximum absolute deviations from the unperturbed baseline were computed for proximity ($\Delta f_1 = \max|f_1(g_i) - f_{1,0}|$) and ship cost ($\Delta J_{\text{cost}} = \max|J_{\text{cost}(g_i)} - \text{Cost}_0|$). To combine both objectives without arbitrary weightings, each deviation was non-dimensionalised by normalising against the base solution's value to produce a composite sensitivity score:

$$\text{Score}(g_i) = \frac{\max|\Delta f_1(g_i)|}{f_{1,0}} + \frac{\max|\Delta J_{\text{cost}(g_i)}|}{\text{Cost}_0} \tag{22}$$

Genes were then ranked in descending order of this composite sensitivity metric, as summarised in Table 11.

Table 11 Local sensitivity ranking and objective excursions across all 13 genotype parameters evaluated on the 46-year ensemble (39 training years plus the 7 test years; $f_{1,0} = 0.898$, $\text{Cost}_0 = \$28,799$).

Rank	Gene	Description	max $\lvert\Delta f_1\rvert$	max $\lvert\Delta$ cost$\rvert$	Score
1	φ_2	Cluster 2 bearing	0.106 (11.8%)	\$3,296 (11.4%)	0.232
2	α_1	Cluster 1 heading	0.147 (16.3%)	\$451 (1.6%)	0.179
3	φ_3	Cluster 3 bearing	0.024 (2.7%)	\$3,910 (13.6%)	0.162
4	w	Edge placement	0.021 (2.3%)	\$1,983 (6.9%)	0.092
5	θ_3	Cluster 3 orientation	0.006 (0.7%)	\$715 (2.5%)	0.032
6	θ_1	Cluster 1 orientation	0.007 (0.8%)	\$370 (1.3%)	0.021
7	d_1	Cluster 1 distance	0.014 (1.5%)	\$131 (0.5%)	0.020
8	θ_2	Cluster 2 orientation	0.000 (0.1%)	\$468 (1.6%)	0.017
9	s_1	Cluster 1 spacing	0.006 (0.7%)	\$132 (0.5%)	0.011
10	s_2	Cluster 2 spacing	0.001 (0.1%)	\$196 (0.7%)	0.008
11	d_2	Cluster 2 range	0.003 (0.3%)	\$124 (0.4%)	0.007
12	s_3	Cluster 3 spacing	0.002 (0.2%)	\$125 (0.4%)	0.007
13	d_3	Cluster 3 range	0.002 (0.2%)	\$46 (0.2%)	0.004

The parameter values above show a clear division between genes that matter and genes that do not. The Cluster 2 bearing φ_2, the Cluster 1 heading α_1 and the Cluster 3 bearing φ_3 are the most sensitive, followed by the edge-relative placement gene w; all other genes score at least a factor of three lower, and the cluster ranges d_k and spacings s_k are an order of magnitude less sensitive. The leading genes act on different objectives. Coverage sensitivity is led by α_1, which moves coverage by up to 0.147 away from the knee point, and φ_2 at 0.106, followed by φ_3 (0.024), w (0.021) and d_1 (0.014); all remaining genes stay within 0.007. Cost deviation is led by φ_3 at \$3,910, then φ_2 at \$3,296 and w at \$1,983 (the edge-tracking leg, which is zero at the knee and grows as the anchor moves west), while the remaining genes move cost by at most \$715.

The coverage response to α_1 is one-sided, and it is set by deployability. Turning the Cluster 1 heading towards due south costs at most 0.013 in coverage, but turning it westward from the knee's 215° swings the first triad towards the ice edge and out of the valid deployment cells: at $\alpha_1 = 230°$ at least one buoy decodes off valid ice in 15 of the 46 years, and at 245° in 29 of them, so the on-ice factor and the constraint together remove up to 0.147 of coverage. The knee therefore sits close to the deployability boundary in α_1, placing Cluster 1 as near to the edge as the on-ice rule allows. The same mechanism contributes to the coverage loss when φ_2 swings west to 239°, which puts buoys off valid ice in 16 of the 46 years. Because no repair step absorbs these displacements, the headings that place the clusters relative to the edge are now where deployability is decided, and they rank accordingly. Macro-cluster

geometry therefore governs spatial dispersion, deployability and ship route length, while micro-cluster spacing and triangle orientation can be adjusted with minimal penalty.

4.3.2 Pairwise interaction surfaces

The pairwise response surfaces shown in Fig. 9 evaluate whether the three leading parameters (φ_2, α_1, and φ_3) interact non-linearly or act independently. Unlike a separable response, in which slicing across one gene yields the same profile at every value of the other, the coverage surfaces (top row) show compounding losses wherever a combination of genes pushes buoys towards the edges of the valid deployment region. The $\varphi_2 \times \alpha_1$ surface is the deepest: coverage falls by up to 0.290 when both headings swing west, more than the sum of the two single-gene losses (0.253), and the joint response departs from the sum of the single-gene responses by up to 0.11 across the grid. The $\varphi_2 \times \varphi_3$ surface is broadly flat near the knee but contains a sharp trough (a loss of up to 0.168) where Cluster 2 turns towards due south ($\varphi_2 \leq 186°$) while Cluster 3 turns east of north ($\varphi_3 \geq 14°$): Cluster 3 then runs into the eastern ROI boundary, where centroid clipping pulls clusters closer than the 50 km inter-cluster minimum and, at the extreme, leaves one buoy off valid ice in every year. The $\varphi_3 \times \alpha_1$ pairing is close to separable (departure from additivity below 0.03) and is dominated by the westward α_1 loss. In every pairing the knee lies on a plateau whose edge, in at least one direction, is a deployability or spacing boundary, so a suboptimal heading cannot be rescued by adjusting a companion gene.

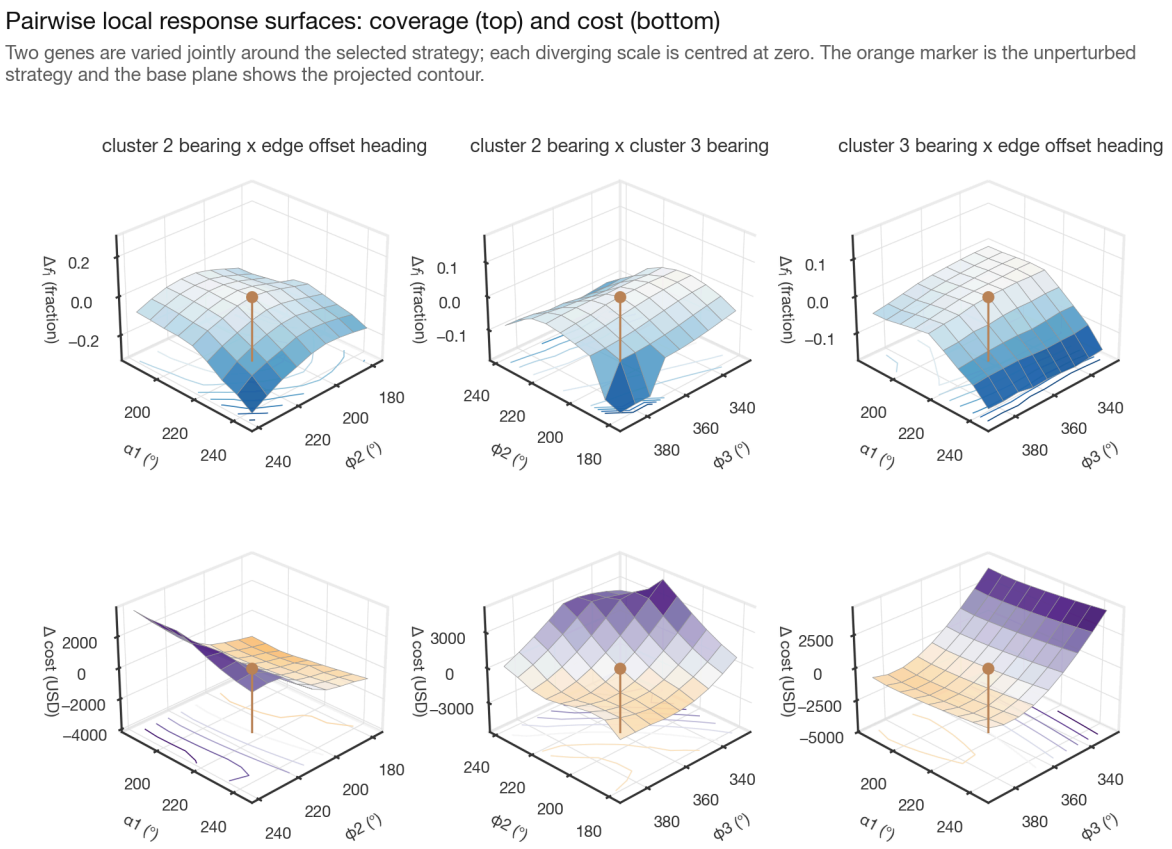


Fig. 9 Pairwise 3D local response surfaces for $\varphi_2 \times \alpha_1$, $\varphi_2 \times \varphi_3$, and $\varphi_3 \times \alpha_1$ on 9 by 9 grids; coverage (top row) and cost in USD (bottom row). Each diverging scale is centred at zero, the orange marker is the unperturbed strategy, the base plane shows the projected contour, and each panel is viewed from the surface's low side so the height field never occludes itself.

The cost surfaces (bottom row) show geometric coupling between the two inter-cluster bearings ($\varphi_2 \times \varphi_3$), whose joint cost response departs from the sum of the single-gene responses by up to \$4.8k, whereas the pairings with α_1 are close to additive in cost. Because transit cost is determined by an open TSP route connecting the deployment locations, displacing both cluster centroids simultaneously alters the

length and orientation of the connecting ship legs jointly, meaning route cost cannot be treated as a simple additive sum of separate heading deviations. Across all pairings, the cost minima do not coincide with the coverage ridges, reinforcing that transit cost and spatial coverage respond to different geometric drivers.

4.3.3 Tolerance to deployment error

A second operational test displaced every buoy drop position with isotropic Gaussian error at $\sigma = 0, 2, 5, 10$ and 20 km, with 50 perturbation samples per level. This is shown in Fig. 10 below. Median robust coverage fell from 0.898 with no error to 0.889 at 2 km, 0.828 at 5 km, 0.791 at 10 km and 0.701 at 20 km. The 5th–95th percentile range (0.861–0.899 at 2 km, 0.745–0.894 at 5 km, 0.686–0.853 at 10 km and 0.615–0.769 at 20 km) shows that individual realisations can lose far more coverage than the median suggests. Median cost stayed within 0.8% of its undisturbed value (R475,190, $28.8k) with error up to 5 km, then rose to R515,784 ($31.3k) at 10 km and R658,150 ($39.9k) at 20 km as displaced buoys lengthen the deployment route.

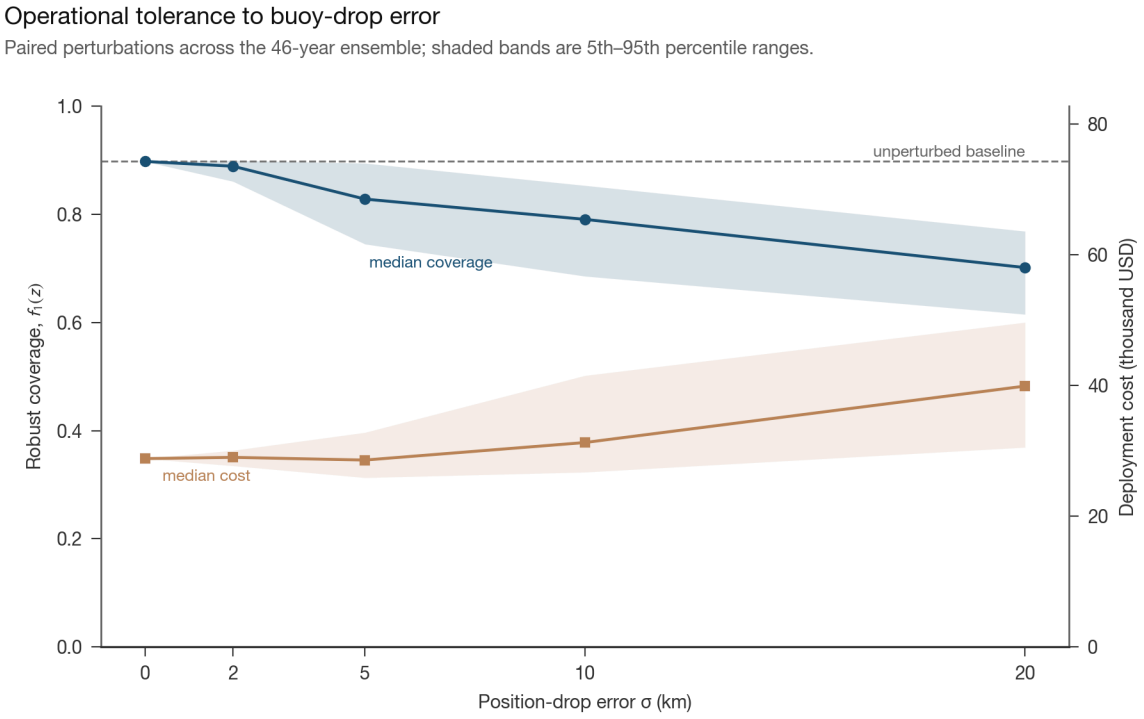


Fig. 10 Operational tolerance to buoy-drop position error. Median robust coverage (blue, left axis) and median deployment cost (orange, right axis) against Gaussian drop error; shaded bands show the 5th–95th percentile ranges across 50 paired perturbations per level.

4.3.4 Operational interpretation

Taken together, the two experiments support a tiered precision policy for deployment operations: the inter-cluster headings (φ_2, φ_3), the Cluster 1 heading (α_1) and the edge-relative placement (w) should be treated as high-precision instructions, while the remaining genes tolerate materially larger deviations without a comparable immediate coverage penalty. The Cluster 1 heading needs an asymmetric tolerance: an error towards due south is cheap, but an error westward, towards the edge, quickly costs deployable positions, so in the field the turn into the pack should err to the south. Expedition tolerances should be set from an acceptable lower-tail coverage loss rather than from the median curve alone. That is, the 5th percentile stays at 0.861 at 2 km error but falls to 0.745 at 5 km and 0.686 at 10 km; if the mission requires coverage above roughly 0.85 with high confidence, drop errors must be kept within 2 km, and even at 5 km the lower tail falls to about 0.75.

4.4 Cross-Product Drift Transfer Validation

The preceding sections assessed the performance of the proposed strategy as it was generalised to unseen years and how it responds to errors in its deployment. This section asks whether the strategy survives a change of drift product. Here, the frozen PP genotype is decoded against the DPGSIV and OSI products' own feature boundaries and is forced through each product's velocity field.

4.4.1 Forcing eligibility

For the forcing to be eligible, trajectory support must reach 75%, and all nine decoded drops must start on product-supported cells. DPGSIV passes both gates in five of the seven test years (2018–2020, 2023 and 2024) and OSI-405-c in four (2018–2020 and 2023). In 2021, feature-relative trajectories retained only 61.0% support under DPGSIV and 53.8% under OSI-405-c, so both failed the forcing-support rule. In 2022 (both products) and 2024 (OSI-405-c), eight of the nine decoded drops landed on product-supported cells and one fell outside, so the deployability gate excluded those years rather than moving the buoy. Over the scored years trajectory support ranged from 90.8% to 99.8% for DPGSIV and from 96.2% to 100.0% for OSI-405-c.

4.4.2 Matched frozen-strategy performance

Fig. 11 below shows the performance of the matched frozen strategy across the different drift products in the four years that were complete in all three products (2018–2020 and 2023).

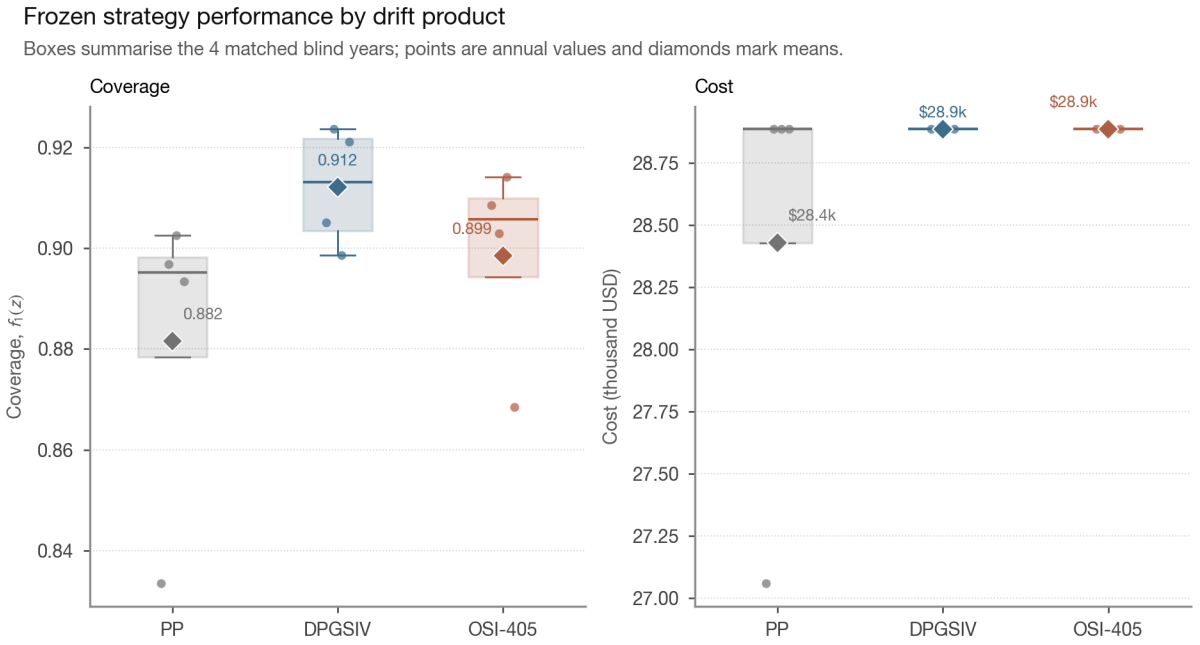


Fig. 11 Matched proposed-strategy performance by drift product. Boxes and whiskers summarise the four years complete in all three products (2018–2020 and 2023), points show annual values, and diamonds with direct labels mark means.

Here, mean penalised coverage was 0.882 under PP forcing, 0.912 under DPGSIV forcing, and 0.899 under OSI-405-c forcing. Relative to the matched PP scores, the mean coverage difference was +0.031 for DPGSIV and +0.017 for OSI-405-c; most of that margin comes from 2018, the atypical-edge test year on which the PP-forced decode is weakest (0.834) while both external decodes remain at their usual level (0.905 and 0.909). In the years all three products can support, the frozen rule performs at least as well under the replacements as under its native forcing. It is also the cheapest strategy in every product, undercutting every reference including the fixed-coordinate draw. Mean matched costs were USD 28,428 for PP and USD 28,885 for both DPGSIV and OSI-405-c, within 2% of one another. Product-relative

decoding moves the deployment geographically, which could change the edge leg and deployment tour of the ship route even though the genes and cost model remain fixed; with the anchor at $w = 0$ there is no edge leg, the array translates rigidly with the product's edge, and the deployment tour is identical in every scored external year. The lower PP mean reflects only the clipped 2018 PP decode ($27.1k).

4.4.3 Comparison with reference deployments

The mean performance for the proposed and baseline strategies in each product is summarised in Table 12 and their distributions are illustrated in Fig. 12. The proposed strategy carries its advantage into both external products: coverage reaches 0.89–0.91 across the three products against 0.39–0.47 for the grid and random draws, 0.31–0.52 for the fixed-coordinate draw and 0.26–0.32 for the 2022-style fan, at $28.6k–$28.9k in every product, undercutting the grid and random references by 42–47%.

Table 12 Cross-product comparison of the frozen feature-relative strategy against the reference deployments, as means over each strategy's eligible years (all seven under PP; five under DPGSIV and four under OSI-405-c for the proposed strategy; six to seven for the references; Section 4.4.1). Cost is in thousands of USD. Random entries average every eligible draw, whereas Table 10 reports the strongest single PP draw.

	Polar Pathfinder		**DPGSIV**		**OSI-405-c**	
Strategy	f_1	Cost ($1000)	f_1	Cost	f_1	Cost
Proposed	0.893	28.6	0.911	28.9	0.899	28.9
Fixed-coord	0.518	32.4	0.314	93.8	0.323	81.2
Random	0.417	51.9	0.419	54.2	0.402	53.4
Grid	0.389	49.4	0.474	53.2	0.465	53.5
Fan (2022-style)	0.316	43.3	0.261	42.7	0.258	42.7

The fixed-coordinate strategy illustrates the failure mode that the feature-relative encoding avoids: although it is eligible in all seven years under both external products, its coverage collapses to zero or near-zero (at most 0.01) away from its 2023 tuning year in 2018–2021 under both products, and only the adjacent years (2022–2024) remain competitive (0.51–0.92 under DPGSIV and 0.57–0.93 under OSI-405-c). The frozen strategy is therefore not merely transferable across drift products but also the optimal strategy within each: it delivers the highest coverage and the lowest cost of every strategy in every product.

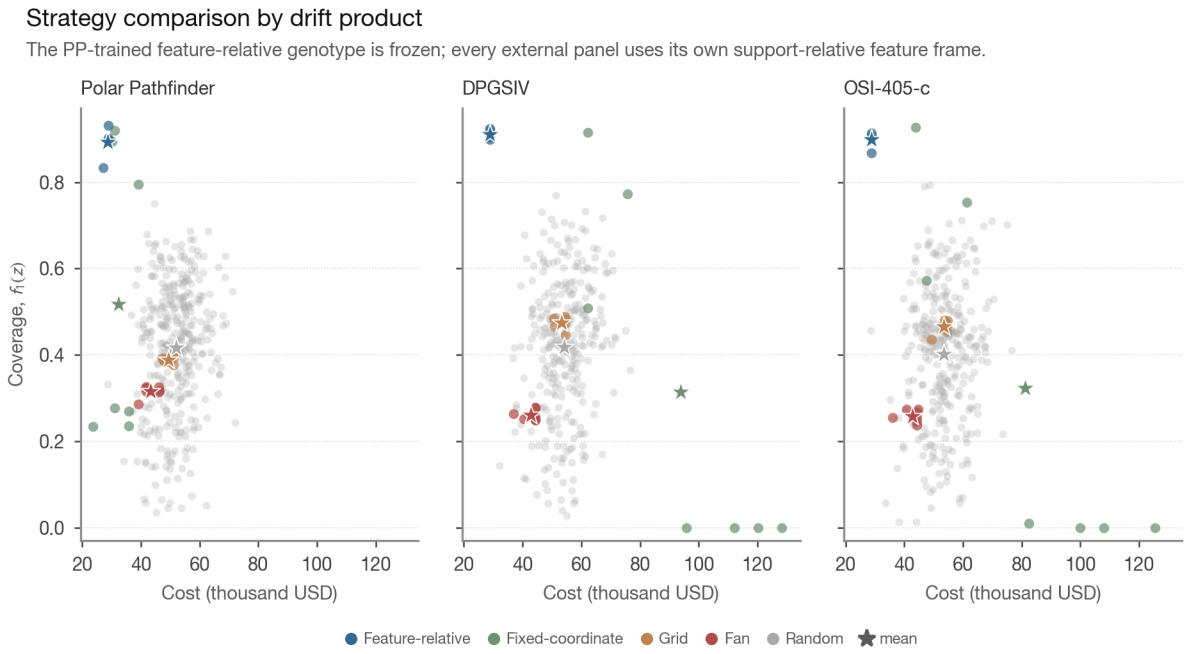


Fig. 12 Coverage–cost comparison for PP, DPGSIV, and OSI-405-c. Colour identifies strategy within each panel; circles are eligible annual or random evaluations and stars mark means. Only evaluations satisfying the product-specific support rules are included.

5 Summary and Conclusion

This work has presented a robust optimisation framework for ice-tethered buoy deployment to maximise drift coverage and minimise cost while maintaining appropriate geometry for DKA. A feature-relative genotype encoding was proposed to address the hindcast-to-forecast problem, allowing a strategy trained on historical ice conditions to generalise to unseen years with their own ice-edge geometry and location. The genotype was decoded into a set of deployment instructions that were relative to the ice edge, rather than absolute coordinates, and the resulting deployment was forced through a 14-day drift simulation to evaluate its coverage and cost. The optimisation framework used a multi-objective evolutionary algorithm to explore the trade-off between coverage and cost, producing a Pareto front of candidate strategies.

The framework was trained on 39 years of historical ice motion and tested on seven unseen years. Deployability was built into the encoding rather than repaired after decoding: the frozen proposed genotype placed all nine buoys on valid ice in every one of the 46 years, and every member of the Pareto front did so in every training year. The 99.4% performance retention of the proposed strategy on blind test years (slightly above 100% excluding the single most atypical test year) demonstrated that this feature-relative strategy enabled pre-cruise planning despite unknown future ice conditions. Accordingly, this addressed a fundamental operational challenge by allowing expedition planners to develop deployment plans in advance with confidence that they would remain valid regardless of the ice conditions encountered at the time of deployment. The strategy also achieved markedly improved coverage – roughly 1.7–2.8 times the usable coverage of four reference deployments, including a fixed-coordinate strategy optimised for a specific year, a regular grid, a random deployment, and a 2022-style fan deployment – at lower cost than all of them (12–45% cheaper).

The strategy remained valid when transferred from training on the PP product to testing on the DPGSIV and OSI-405-c drift products in the years those products can support. This successful transfer across alternative external drift products provided evidence that the proposed approach generalised, rather than that its blind-year performance had a narrow PP-product explanation. The frozen genes continued to define valid, low-cost arrays after the environmental feature, GPS deployment locations, and 14-day motion fields were replaced. Absolute coverage in the external products reached 0.911 (DPGSIV,

five eligible years) and 0.899 (OSI-405-c, four eligible years), at or slightly above the PP-forced 0.893 and far above the references; in each product the frozen strategy undercut the grid and random references by 42–47% on cost while delivering roughly twice their coverage. In three product-years a single one of the nine frozen drops fell outside the external product's support and the year was excluded, a reminder that a strategy planned on one product's ice mask should be checked against the ice actually observed at deployment.

The local robustness analysis complemented this result, using the response-surface test to investigate how well the strategy tolerated variations in the accuracy with which deployments followed its instructions. Notably, the most sensitive genes were the inter-cluster headings (φ_2, φ_3), the Cluster 1 heading (α_1) and the edge-relative placement (w) that defined the chained cluster geometry and its position relative to the edge. The same sequential encoding that made the product transfer work also concentrated the operational risk in a small, identifiable subset of instructions. Navigation and deployment location verification effort should target these instructions rather than imposing one strict tolerance on every parameter. The deployment-error experiment then bounded how much of the validated performance survived realistic placement inaccuracy: median coverage degraded smoothly. With deployment-position errors of $\sigma = 5$ km, 5th percentile perturbations fell to 0.75 coverage even though the median remained near 0.83; at $\sigma = 2$ km, however, the 5th percentile was 0.86, close to the undisturbed 0.90. If high confidence in coverage above roughly 0.85 is required, deployment-location errors should be kept within 2 km.

Overall, the Pareto knee point used as the case study for the results in this paper provided a balanced starting point for expedition planners. However, for fixed budgets, the highest-coverage solution below the cost threshold should be chosen.

Acknowledgment

During the preparation of this work the authors used Claude Code and OpenCode GO to assist with developing the analysis code used to implement the optimisation framework and generate the plots above. After using these tools, the authors reviewed and edited the content as needed and take full responsibility for the content of the published article.

References

[1] J. Weiss and V. Dansereau, "Linking scales in sea ice mechanics," *Philosophical Transactions of the Royal Society A: Mathematical, Physical and Engineering Sciences*, vol. 375, no. 2086, p. 20150352, Feb. 2017, doi: 10.1098/rsta.2015.0352.

[2] T. Tian, A. Fraser, T. Lavergne, S. Fiddes, C. Zhao, and P. Heil, "Linking timescale-dependent Antarctic sea ice kinematic observations to ice thickness," *Remote Sensing of Environment*, vol. 298, p. 113813, Dec. 2023, doi: 10.1016/j.rse.2023.113813.

[3] C. Ning, S. Xu, Y. Zhang, X. Wang, Z. Fan, and J. Liu, "Lagrangian tracking of sea ice in Community Ice CodE (CICE; version 5)," *Geoscientific Model Development*, vol. 17, no. 17, pp. 6847–6866, Sep. 2024, doi: 10.5194/gmd-17-6847-2024.

[4] J. Hutchings, A. Roberts, C. Geiger, and J. Richter-Menge, "Spatial and temporal characterization of sea-ice deformation," *Annals of Glaciology*, vol. 52, no. 57, pp. 360–368, Jan. 2011, doi: 10.3189/172756411795931769.

[5] J. K. Hutchings, A. C. Bliss, D. Mondal, and P. Elosegui, "Sea Ice Deformation Is Not Scale Invariant Over Length Scales Greater Than a Kilometer," *Geophysical Research Letters*, vol. 51, no. 12, p. e2024GL108582, Jun. 2024, doi: 10.1029/2024GL108582.

[6] P. Rampal, J. Weiss, D. Marsan, R. Lindsay, and H. Stern, "Scaling properties of sea ice deformation from buoy dispersion analysis," *Journal of Geophysical Research: Oceans*, vol. 113, no. C3, Mar. 2008, doi: 10.1029/2007JC004143.

[7] D. Marsan, H. Stern, R. Lindsay, and J. Weiss, "Scale dependence and localization of the deformation of Arctic sea ice," *Physical Review Letters*, vol. 93, no. 17, p. 178501, Oct. 2004, doi: 10.1103/physrevlett.93.178501.

[8] A. Womack, A. Alberello, M. de Vos, A. Toffoli, R. Verrinder, and M. Vichi, "A contrast in sea ice drift and deformation between winter and spring of 2019 in the Antarctic marginal ice zone," *The Cryosphere*, vol. 18, no. 1, pp. 205–229, Jan. 2024, doi: 10.5194/tc-18-205-2024.

[9] H. L. Stern and R. W. Lindsay, "Spatial scaling of Arctic sea ice deformation," *Journal of Geophysical Research: Oceans*, vol. 114, no. C10, 2009, doi: 10.1029/2009JC005380.

[10] R. Molinari and A. D. Kirwan, "Calculations of Differential Kinematic Properties from Lagrangian Observations in the Western Caribbean Sea," *Journal of Physical Oceanography*, vol. 5, no. 3, pp. 483–491, Jul. 1975, doi: 10.1175/1520-0485(1975)005<0483:CODKPF>2.0.CO;2.

[11] M. Plante *et al.*, "A sea ice deformation and rotation rate dataset (2017–2023) from the Environment and Climate Change Canada automated sea ice tracking system (ECCC-ASITS)," *Earth System Science Data*, vol. 17, no. 2, pp. 423–434, Feb. 2025, doi: 10.5194/essd-17-423-2025.

[12] W. Hibler, W. Weeks, A. Kovacs, and S. Ackley, "Differential sea-ice drift. I. Spatial and temporal variations in sea-ice deformation," *Journal of Glaciology*, vol. 13, no. 69, pp. 437–455, Jan. 1974, doi: 10.3189/s0022143000023212.

[13] M. Uusinoka, J. Haapala, J. Åström, M. Lensu, and A. Polojärvi, "Scale invariance in kilometer-scale sea ice deformation," *The Cryosphere*, vol. 19, no. 12, pp. 6493–6506, Dec. 2025, doi: 10.5194/tc-19-6493-2025.

[14] M. A. Tschudi, W. N. Meier, and J. S. Stewart, "An enhancement to sea ice motion and age products at the National Snow and Ice Data Center (NSIDC)," *The Cryosphere*, vol. 14, no. 5, pp. 1519–1536, May 2020, doi: 10.5194/tc-14-1519-2020.

[15] L. Newman *et al.*, "Delivering sustained, coordinated and integrated observations of the Southern Ocean for global impact," *Frontiers in Marine Science*, vol. 6, p. 433, Aug. 2019, doi: 10.3389/fmars.2019.00433.

[16] S. Swart *et al.*, "Constraining Southern Ocean Air-Sea-Ice Fluxes Through Enhanced Observations," *Frontiers in Marine Science*, vol. 6, p. 421, Jul. 2019, doi: 10.3389/fmars.2019.00421.

[17] M. de Vos, C.-L. Ramjukadh, M. de Villiers, C. Lyttle, A. Womack, and M. Vichi, "Polar Iridium Surface Velocity Profilers (p-iSVP), and standard Iridium Surface Velocity Profilers (iSVP) during SCALE 2019 Winter and Spring Cruises." [Online]. Available: https://zenodo.org/record/7954779

[18] A. L. Kohout, M. Smith, L. A. Roach, G. Williams, F. Montiel, and M. J. M. Williams, "Observations of exponential wave attenuation in Antarctic sea ice during the PIPERS campaign," *Annals of Glaciology*, vol. 61, no. 82, pp. 196–209, Sep. 2020, doi: 10.1017/aog.2020.36.

[19] A. Kohout, M. Williams, M. Smith, G. Williams, L. Roach, and S. Ackley, "PIPERS Waves in Ice Observations, version 1." [Online]. Available: http://dx.doi.org/10.17632/b33xxnpfyw.1

[20] C. Eayrs *et al.*, "SA Agulhas II Winter 2017 Cruise: Waves In Ice Observation Systems (WIIOS), version 1." [Online]. Available: http://dx.doi.org/10.26179/5cc934992f065

[21] K. Machutchon *et al.*, "SA Agulhas II Winter 2017 Cruise: ice edge drifters." [Online]. Available: http://dx.doi.org/10.26179/5cc937513bd6d

[22] P. Heil, J. Hutchings, R. Stevens, and O. Lecomte, "In situ Lagrangian drifting buoy data off East Antarctica for the austral spring of 2012, deployed during the SIPEX II voyage of the Aurora Australis, version 1." [Online]. Available: https://data.aad.gov.au/metadata/SIPEX_II_Buoys

[23] M. J. Doble and P. Wadhams, "Dynamical contrasts between pancake and pack ice, investigated with a drifting buoy array," *Journal of Geophysical Research: Oceans*, vol. 111, no. C11, Oct. 2006, doi: 10.1029/2005JC003320.

[24] X. Zeng *et al.*, "Use of Observing System Simulation Experiments in the United States," *Bulletin of the American Meteorological Society*, vol. 101, no. 8, pp. E1427–E1438, 2020, doi: 10.1175/BAMS-D-19-0155.1.

[25] F. Gasparin *et al.*, "Requirements for an integrated in situ Atlantic Ocean observing system from coordinated observing system simulation experiments," *Frontiers in Marine Science*, vol. 6, p. 83, 2019, doi: 10.3389/fmars.2019.00083.

[26] C. Mao, R. R. King, R. Reid, M. J. Martin, and S. Good, "Assessing the potential impact of changes to the Argo and moored buoy arrays in an operational ocean analysis system," *Frontiers in Marine Science*, vol. 7, p. 588267, 2020, doi: 10.3389/fmars.2020.588267.

[27] B. Paul, B. Baduru, J. Prajapati, V. Daiya, C. Athul, and A. Paul, "Optimising the design of an observational testbed using observing system simulation experiments: a case study in the southeastern Arabian Sea," *Quarterly Journal of the Royal Meteorological Society*, vol. 152, no. 775, p. e70069, 2025, doi: 10.1002/qj.70069.

[28] N.-H. Kim, D. Baek, J.-il Kwon, J.-Y. Choi, and K.-Y. Heo, "Strategy for additional buoy array installation in operational buoy-observation network in Korea," *Ocean Engineering*, vol. 266, p. 112746, Dec. 2022, doi: 10.1016/j.oceaneng.2022.112746.

[29] I. Rosso *et al.*, "Southern Ocean biogeochemical float deployment strategy, with example from the Greenwich meridian line (GO-SHIP A12)," *Journal of Geophysical Research: Oceans*, vol. 124, no. 1, pp. 403–431, 2019, doi: 10.1029/2018jc014059.

[30] Y. Fujii *et al.*, "Observing System Evaluation Based on Ocean Data Assimilation and Prediction Systems: On-Going Challenges and a Future Vision for Designing and Supporting Ocean Observational Networks," *Frontiers in Marine Science*, vol. 6, p. 417, 2019, doi: 10.3389/fmars.2019.00417.

[31] M. Tschudi, W. Meier, J. Stewart, C. Fowler, and J. Maslanik, "Polar Pathfinder Daily 25 km EASE-Grid Sea Ice Motion Vectors, version 4." [Online]. Available: http://nsidc.org/data/NSIDC-0116/versions/4

[32] EUMETSAT OSI SAF, "OSI SAF Global Low Resolution Sea Ice Drift, OSI-405-c." [Online]. Available: https://user.eumetsat.int/catalogue/EO:EUM:DAT:MULT:GBL-LR-SIDR

[33] N. Kimura and T. Sugimura, "Daily Polar Gridded Sea Ice Velocity." [Online]. Available: https://doi.org/10.17592/001.2025112601

[34] K. Deb, A. Pratap, S. Agarwal, and T. Meyarivan, "A fast and elitist multiobjective genetic algorithm: NSGA-II," *IEEE Transactions on Evolutionary Computation*, vol. 6, no. 2, pp. 182–197, Apr. 2002, doi: 10.1109/4235.996017.

[35] P. Heil *et al.*, "Tidal forcing on sea-ice drift and deformation in the western Weddell Sea in early austral summer, 2004," *Deep Sea Research Part II: Topical Studies in Oceanography*, vol. 55, no. 8–9, pp. 943–962, Apr. 2008, doi: 10.1016/J.DSR2.2007.12.026.

[36] V. A. Squire, "Marginal ice zone dynamics," *Philosophical Transactions of the Royal Society A: Mathematical, Physical and Engineering Sciences*, vol. 380, no. 2235, p. 20210266, Sep. 2022, doi: 10.1098/rsta.2021.0266.

Appendix A. Candidate Coverage Formulations

Five candidate base-coverage formulations were evaluated before the mean minimum distance metric of Section 2.2.3 was adopted. This appendix records their definitions, the behaviour each exhibits under optimisation, and the reasoning that led to the metric selected at each stage. Throughout, the deployment ROI is discretised into N grid cells with centroids $\boldsymbol{g}_k$ $(k = 1, ..., N)$; the n_B buoys follow simulated trajectories $\boldsymbol{r}_b(t_j)$ $(b = 1, ..., n_B,\ j = 1, ..., T)$; and

$$d_k = \min_{b,j} \left\| \boldsymbol{r}_b(t_j) - \boldsymbol{g}_k \right\|_2 \tag{23}$$

is the distance from cell k to the nearest trajectory point. A cell is counted as visited, and its visit count defined, from a search radius r (typically half a grid-cell width):

$$V_k = \begin{cases} 1 \text{ if } d_k \le r \\ 0 \text{ otherwise,} \end{cases} \quad n_k = \sum_{b=1}^{n_B} \sum_{j=1}^{T} \mathbf{1}\Big(\left\| \boldsymbol{r}_b(t_j) - \boldsymbol{g}_k \right\|_2 \le r \Big). \tag{24}$$

Each candidate is evaluated in expectation over the ensemble of drift realisations, $\bar{J}_i = \frac{1}{K} \sum_{k=1}^{K} J_i^{(k)}$. In this work the ensemble analogue is the 39-year training climatology of Section 2.2.4.

J1: Simple Coverage Fraction

A cell counts as covered if any trajectory point falls within r, and the objective is the covered fraction of the ROI:

$$J_1 = \frac{1}{N} \sum_{k=1}^{N} V_k. \tag{25}$$

This is the most direct reading of "spatial coverage", i.e., the fraction of the region a buoy reached at least once during the time period. Under optimisation, however, it behaves as a plateau-and-cliff landscape. Because V_k is a step, a buoy passing just outside r scores identically to one passing hundreds of kilometres away, so near-misses carry no signal, and r is an arbitrary free parameter with no physical basis. With roughly 40 cells and nine buoys the score can take only integer multiples of $\frac{1}{N}$, and the search receives almost no selection gradient. A cell grazed at distance $r - \varepsilon$ also counts as fully covered, so the metric records nothing about how well a cell was sampled. J1 was rejected on these grounds.

J2: Mean Minimum Distance

The metric adopted in this work, defined in Eqs. 4–5 and repeated here for completeness:

$$J_2 = 1 - \frac{1}{N d_{\max}} \sum_{k=1}^{N} d_k. \tag{26}$$

J2 asks, for every cell, how close the nearest trajectory came, and averages those answers across the ROI. It is therefore dominated by what is not covered rather than by how much track was laid down: a few cells sitting far from every trajectory depress the score regardless of how thoroughly the remaining cells were sampled, and redundant near-parallel tracks are discounted because each cell credits only its nearest encounter. It has three other primary strengths: First, it is smooth and graded, so every incremental improvement anywhere in the array changes the score. It introduces no tuning parameter, since $d_{\max}$ is a normaliser rather than a threshold. And it rewards partial progress towards difficult cells, which matters once the ROI relocates each year with the ice edge and perfection is unattainable. Its known limitation is the converse of its strength: a mean tolerates a small number of large holes when everything else is excellent, a shortcoming that must instead be addressed by the explicit geometric penalties of the composite objective (Section 2.2.3).

J3: Ensemble Spread

Dispersion-based objectives reward configurations whose trajectories separate widely, on the reasoning that a larger buoy cloud samples more of the marginal ice zone. Three variants were considered: the maximum separation that any pair attains at any time,

$$J_3^{\max} = \frac{1}{s_{\max}} \max_{t_j} \max_{b<b'} d_{bb'}(t_j), \tag{27}$$

its time average,

$$J_3^{\text{mean}} = \frac{1}{T s_{\max}} \sum_j \max_{b<b'} d_{bb'}(t_j), \tag{28}$$

which favours configurations that stay separated rather than separate only briefly; and the mean pairwise divergence,

$$J_3^{\text{div}} = \frac{2}{T n_B (n_B - 1) s_{\max}} \sum_{j=1}^{T} \sum_{b<b'} \left\| \boldsymbol{r}_b(t_j) - \boldsymbol{r}_{b'}(t_j) \right\|_2. \tag{29}$$

All three were rejected, for three reasons. First, dispersion is a property of the ensemble rather than of the region, meaning that buoys could separate greatly while collectively drifting away from the ice edge, so the objective is blind to the quantity being maximised. Second, large separation is not the same as useful deformation geometry. The strain-rate tensor is inverted from the evolving inter-buoy geometry, so the triangle distorting is itself the measurement, and DKA is not served by unbounded spread. Third, divergence is largely a property of the velocity field; the deployment only controls where it is seeded, so J3 is a weak lever for an algorithm that can only move positions.

J4: Visit Uniformity

A fairness criterion over sampling effort, defined from the visit counts as

$$J_4 = 1 - \frac{\sigma_n^2}{\sigma_{n,\max}^2}, \quad \sigma_n^2 = \frac{1}{N} \sum_{k=1}^{N} (n_k - \bar{n})^2, \tag{30}$$

or, alternatively, in entropy form, $J_{4'} = \frac{-\sum_k p_k \log p_k}{\log} N$ with $p_k = \frac{n_k}{\sum_j n_j}$. Both are maximised by even sampling. J4 cannot lead a search because it is indifferent to whether cells are visited at all: a uniformly zero visit count is perfectly uniform, and therefore scores maximally. It is a rebalancing criterion for a deployment that already covers the region, and at nine buoys over fourteen days across roughly 40 cells the visit counts are far too sparse for a variance or an entropy to be informative. J4 could complement J2, but it cannot replace it.

J5: Minimax Distance

Worst-case proximity, set by the single least-covered cell:

$$J_5 = 1 - \frac{1}{d_{\max}} \max_k d_k. \tag{31}$$

J5 encodes the guarantee that no cell is left behind, and is scientifically attractive for that reason. It is nevertheless hostile to optimisation: the score is decided by one cell, so any buoy movement that does not affect that cell leaves the fitness unchanged. The landscape is flat almost everywhere, and a single bad cell vetoes every other improvement. J5 was therefore rejected as a search objective; it is defined here only to make explicit the worst-case limitation that the adopted mean does not address.

Table 13 summarises how the five candidates compare against the requirements of this problem.

Table 13 Comparison of candidate base-coverage formulations on the properties that matter for a multi-decadal evolutionary search.

Metric	Interpretation	Free parameter	Behaviour under optimisation	Verdict
J_1	Thresholded reach	r (arbitrary)	Step landscape with cliffs at r; near-misses invisible; almost no selection gradient at this grid size	Rejected
J_2	Mean gap to nearest track	None ($d_{\max}$ is a normaliser)	Smooth everywhere; every move changes the score; retains partial progress	Adopted
J_3	Ensemble size	$s_{\max}$	Smooth, but blind to the region and a weak lever on deployment positions	Rejected
J_4	Fairness of effort	None	Zero visits everywhere scores perfectly; counts too sparse at nine buoys over fourteen days	Rejected
J_5	Worst gap	None	Unchanged except at the worst cell; one cell vetoes every other improvement	Rejected; diagnostic only

The mean minimum distance metric was selected because it is the only candidate that satisfied all three requirements simultaneously. First, it supplies a gradient so that every incremental improvement anywhere in the array changes the score, whereas J_1 discriminates only across its threshold, J_5 responds only when the worst cell changes, and J_4 is dominated by noise at this sampling density. This smoothness is also what makes the gene-sensitivity analysis of Section 4.3 meaningful, since a metric with step-like behaviour would leave most gene perturbations invisible. Second, it measures the quantity the deployment actually targets, namely proximity of observations to every part of the ice-edge zone. J_3 optimises the geometry of the buoy ensemble instead, which is neither the coverage goal nor the requirement of differential kinematic analysis. Third, it aggregates robustly over the 39-year training climatology: it degrades gracefully as the ice edge relocates between years and requires no per-year threshold retuning, unlike the radius r on which J_1 and J_4 depend. A further property supports this choice: because the deployment ROI is a fixed-size rectangle anchored to the ice edge (Section 2.1.3.1), the normaliser $D_{\max} \approx 257$ km is constant across the climatology, so years with widely different ice-edge positions remain comparable without retuning and the multi-decadal mean is well defined.

Two consequences of this choice are handled outside the objective. Averaging tolerates isolated large gaps when the remaining cells are well covered, a limitation stated explicitly above through the minimax formulation J_5 but not carried into the search. Redundant, near-parallel trajectories are also penalised implicitly rather than explicitly, since each cell credits only its nearest encounter; the inter-cluster spacing term (v_{inter}; Section 2.2.3) addresses the same concern at the level of cluster placement.